ROYAL INSTITUTE
OF TECHNOLOGY

Electromagnetic Simulation, Analysis and Design with Application to Antennas and Radar Absorbers

ALIREZA MOTEVASSELIAN

Doctoral Thesis
Stockholm, Sweden 2012

KTH School of Electrical Engineering
ISSN 1653-5146 SE-100 44 Stockholm
ISBN 978-91-7501-481-4 SWEDEN

Akademisk avhandling som med tillstånd av Kungl Tekniska högskolan framlägges till offentlig granskning för avläggande av teknologie doktorsexamen fredagen den 5 oktober 2012 klockan 13.15 i sal F3, Kungl Tekniska högskolan, Lindstedtsvägen 26, Stockholm.

Tryck: Universitetsservice US AB

Abstract

The present thesis considers two different subjects in the research area of electromagnetics. The first part is concerned with antenna design and the second with radar absorbers and rasorber.

In the first part, a novel excitation technique for cylindrical dielectric resonator antennas is introduced to produce circular polarization. The exciter is a tape helix that is wound around the dielectric resonator and is fed by a coaxial probe. The helix excites the $HE_{11\delta}$ modes in phase quadrature in the cylindrical dielectric resonator antenna. The height of the helix is determined using the Hansen-Woodyard condition for an end-fire array based on the phase velocity of the surface wave traveling along the dielectric resonator side wall. This phase velocity is estimated from the phase velocity in an infinitely long dielectric rod with the same permittivity and radius as the dielectric resonator antenna. The helical exciter is required to operate in the helix axial mode. The height of the helix is usually taller than the height of the dielectric resonator core. Using this type of excitation, a 3 dB axial-ratio bandwidth of 6.4% was achieved for a sample design with dielectric constant $\varepsilon_r \sim 11$. The achieved 3 dB axial-ratio bandwidth is greater than that typical of other reported single feed cylindrical dielectric resonator antennas. A prototype of the sample design is fabricated and measured and a good agreement between simulation and measurement is observed. Furthermore, two approaches for the enhancement of the 3 dB axial ratio bandwidth are proposed: removing the central portion of the cylindrical dielectric resonator and using stacked cylinders. The advantages and limitations of each approach are discussed. Another perspective on the proposed design is to consider the antenna as a helix with a dielectric resonator core. In this perspective, the effects of the dielectric core on the helix antenna are discussed.

The second part of the thesis is concerned with the design of thin wideband electromagnetic planar absorber for X- and KK_u-band which also has a polarization sensitive transparent window at frequencies lower than L-band. The design is based on a two layer capacitive circuit absorber with the backmetal layer replaced with a polarization sensitive frequency selective surface. The structure is studied for normally incident waves with two orthogonal linear polarizations. The structure is optimized to have high transparency at low frequencies for one of the polarizations and at the same time good absorption efficiency for both polarizations at the high-frequency band. For one of the polarizations a -1.9 dB transmission with a transmission loss of less than 10% at 1 GHz as well as a 2.25:1 (75%) bandwidth of -20 dB reflection reduction are achieved. For the other polarization we obtained more than 3:1 (100%) bandwidth of -19 dB absorption. Compared with our earlier design based on a Jaumann absorber, we succeed in significantly reducing the transmission loss at the transparent window. Furthermore, the module of absorption quality is extensively improved. The improvements are based on using periodic arrangements of resistive patches in the structure design. The investigation of the structure for oblique angles of incidence and non-ideal materials is also accomplished.

Acknowledgements

I would like to express my deep and sincere gratitude to my supervisor Lars Jonsson. I appreciate all his contributions of time, ideas and encouragements during my PhD study. It has been an honor for me to be his first PhD student. I am thankful of his patience and support at every stage of this PhD work.

This thesis, particularly in the second part, would not have been possible without the help of my colleague, Anders Ellgardt. I would like to record my gratitude to him for his advice, guidance and great ideas in several aspects of my research. It would be always a good memory in my mind, the pleasant time in our shared office.

I am also grateful to my co-supervisor Martin Norgren for his valuable participation in part of the work as well as helpful comments and hints for the courses I have had with him. Martin, with his great electromagnetic knowledge, is always a worthy reference at the department.

This thesis arose in part out of years of research done since I came to the Electromagnetic Theory Group at KTH. By that time, I have worked with a great number of people whose kind contributions have aided me in several aspects of research, courses, and also in general life in Sweden. It is a pleasure to convey my gratitude to them all in my humble acknowledgments. To mention a few, in the first place I would like to our computer administrator, Peter Lönn, for his kind technical support with computer hardware and software. Furthermore, I thank all present and former colleagues at the department for good time I had with them during lunch time and coffee breaks and their contribution to the nice atmosphere. I am also thankful to all my friends here and in my home country who have been my resource of encouragement.

Finally, I wish to thank my parents, my sister Mahtab, my cousins Abbas and Nadereh, and also my dear Azadeh for their great love to me and for aiding me a lot to accept and enjoy my new life conditions in Sweden.

Alireza Motevasselian
Stockholm, September 2012

Contents

Chapter 1

Introduction

The present thesis is concerned with two different problems from two distinct subjects in the research area of electromagnetics. The first part is the most recent work and is related to antenna design. This part of the PhD work was supported by The Swedish Governmental Agency for Innovation Systems (VINNOVA) within the VINN Excellence Center Chase and the IMT-advanced and beyond project 2011-03867. The second part is related to my former research on radar cross section reduction, radar absorber and rasorber design. A larger portion of this part, including the shape optimization and curved Jaumann absorbers, was done in my Licentiate thesis [1] under an NFFP 4 SIGANT project. The continuance and modification of that work is discussed in the second part of this thesis.

Part I of this thesis offers a general introduction to dielectric resonator antennas (DRAs) excited by an external conducting helix. This part contains five separate chapters. The first chapter provides a history of DRAs together with some theoretical knowledge on cylindrical dielectric rods and resonators that are used in the design process. A brief introduction to the helix is presented in the second chapter of this part. In the third chapter the dielectric rods and tubes are analytically investigated to determine the phase velocity of the guiding wave supported by these waveguides. In the fourth chapter, polarization and its different kinds are defined and discussed. This part ends with presenting the proposed design, its characteristics, and presents some conclusions in the forth section.

In Part II, the discussion is about a radar absorber design with a transparent window. This part also contains five chapters. In the first chapter of this part, after providing a background information on radar absorbers, the design problem is stated. Then in the second chapter of Part II, a brief discussion concerning the methods employed in the design process is provided. In the third and fourth chapter of this part, Jaumann and capacitive circuit rasorber design are described. This part closes with a discussion of the contributions and results and a conclusion.

This thesis is followed with Part III, which contains selected journal and con-

ference papers of the author that define the subject of this thesis. The first three papers are related to the DRA design. The fourth paper is on an investigation on DRA arrays. The last two papers are on the radar absorber part. The papers are summarized as follows:

In **Paper I**, a circularly polarized cylindrical dielectric resonator antenna excited by an external tape helix is presented. A prototype of the proposed configuration is fabricated and measured. Measured and simulated return loss, axial ratio, and the radiation pattern are presented and discussed. Design guidelines for this type of antenna are also provided. The proposed excitation method for cylindrical dielectric resonator antennas is uncomplicated and easy to fabricate, while offering a 6.4% axial-ratio bandwidth, which is more than that reported in the literature for the typical axial-ratio bandwidth of single feed dielectric resonator antennas.

In **Paper II**, the external helical exciter is used to excite a hollow cylindrical dielectric resonator antenna to generate circular polarization. Design guidelines are provided and three design cases are presented. A prototype for one of the designs is fabricated and measured. Measured and simulated data are presented and discussed. It is shown that both the impedance and the 3 dB axial ratio bandwidth increase as the wall thickness of the hollow cylindrical dielectric resonator decreases. However, the reduction in the wall thickness also results in a greater height for the helix exciter.

In **Paper III**, a stacking method is used to enhance the 3 dB axial ratio and impedance bandwidth of the circularly polarized cylindrical dielectric resonator antennas excited by an external tape helix. In this method, a dielectric cylinder with lower permittivity than the basement cylindrical dielectric resonator is placed concentrically on top of the basement cylinder. This configuration offers an axial ratio bandwidth up to 11% and impedance bandwidth of 31%.

In **Paper IV**, a comparison in radiation patterns and mutual coupling between finite and infinite square lattice arrays of dielectric resonator antenna (DRA) elements is done. The array elements are cavity backed, slot fed cylindrical DRAs that utilize the $HE_{11\delta}$ mode. It can be observed that the degree of mutual coupling for the non-edge elements is very close to the mutual coupling between the corresponding elements in the infinite array. However, a large difference can be observed in the mutual coupling between the center element and the two corner elements in the finite array compared to the corresponding elements is the infinite array. The coupling is strongest in the E-plane and it is shown how it changes the embedded element patterns in the array.

Paper V presents an investigation on a Jaumann absorber, where its metal backing is replaced with a combined low-pass and polarizer FSS. The structure is optimized with respect to the absorption and polarization-dependent low-frequency transparency properties. This structure is bent to be used in an idealized curved wing-front end. The monostatic radar cross-section of the curved structure is determined and presented for two orthogonal linearly polarized incident plane waves.

It is shown that the FSS-Jaumann structure preserves an absorption similar to the planar Jaumann absorber.

Finally, in **Paper VI** a thin wide-band electromagnetic planar rasorber for X- and K_u-bands is presented. This rasorber has a polarization sensitive transparent window at frequencies lower than L-band. The design is based on a two layer capacitive circuit absorber with the back-metal layer replaced with a polarization sensitive frequency selective surface. This structure is studied for normal incident waves with two orthogonal linear polarizations. We optimized the structure to obtain high transparency at low frequencies for one of the polarizations and at the same time good absorption efficiency for both polarizations at the high-frequency band. The transmission loss is significantly reduced compared to our earlier design based on a Jaumann absorber. Furthermore, the module of absorption quality is extensively improved. The structure is also investigated for oblique angles of incidence and non-ideal materials.

The main part of the work in all the papers included in this thesis was done by the thesis author. Lars Jonsson helped me with the proof reading of the papers and provided me with valuable suggestions. For **Paper I** and **Paper II**, Anders Ellgardt helped me in the fabrication of the antenna prototypes and measurement process. He also contributed to the proof reading of **Paper I**, **Paper II**, and **Paper IV**.

Part I

General Introduction to Circularly Polarized Dielectric Resonator Antennas Using Helical Excitation

Chapter 2

Dielectric Resonator Antennas (DRAs)

2.1 History and Background

The use of dielectric rods as waveguides was first investigated more than a century ago by Hondros and Debye [2]. Propagation in dielectric waveguides differs from propagation in hollow metal tubes in many aspects, and in particular in the existence of electromagnetic fields outside the dielectric guides, whereas the fields are entirely confined within a metal tube waveguides. The radiation loss as well as the loss due to a rather high loss in dielectric materials made dielectric waveguides less attractive for transmission system designers. The development of metal tubes completely suppressed investigations on dielectric waveguides. It was mainly due to the fact that the electromagnetic energy is entirely contained within the surrounding metallic surface in metal tube waveguides, whereas it also exists outside dielectric waveguides that leads to a greater transmission loss due to radiation when they bend and at discontinuities in the waveguide.

The radiation characteristics of the dielectric waveguide attracted researchers' attention to the use dielectric rods as a directional radiator. The early works of Mueller and Tyrrel [3] and Halliday and Kiely [4], theoretically and experimentally investigated the radiation from dielectric rods. More detailed investigations on the radiation mechanism of dielectric rods were carried out by Watson and Horton in [5] and also the works presented in [6, 7].

Dielectric materials have also been used as resonators. Dielectric resonators was first introduced in 1939 by Richtmyer [8]. They were, however, in little use for about 30 years. With the development of low-loss ceramic materials in the late 1960s, dielectric materials began to be used as high quality factor microwave resonator elements, such as filters and oscillators. They offer a more compact alternative than metallic cavities and also a compatible technology for integration with printed circuits [9, 10].

Similar to dielectric waveguides, unshielded dielectric resonators radiate electromagnetic fields. The radiated fields of dielectric resonators was investigated by Van Bladel in 1975 [11]. In 1983 Long, McAllister and Shen introduced cylindrical [12], rectangular [13] and hemispherical [14] dielectric resonators as efficient radiators and provided the first systematic theoretical and experimental investigation on dielectric resonator antennas (DRAs). Since then, intensive research efforts have been dedicated to this concept. Excitation techniques [15–18], bandwidth enhancement [19–22], DRAs with special shapes [23–28], and the polarization characteristics [29–35] have been the most popular subjects in the DRA research area.

2.2 Cylindrical DRA

Among the three basic shapes of DRAs, rectangular, cylindrical, and spherical, the cylindrical shaped DRA has been the most popular shape studied for practical antenna applications [36, 37]. A cylindrical DRA is characterized with a radius, a, height, h, and dielectric constant, ε_r as shown in Fig. 2.1.

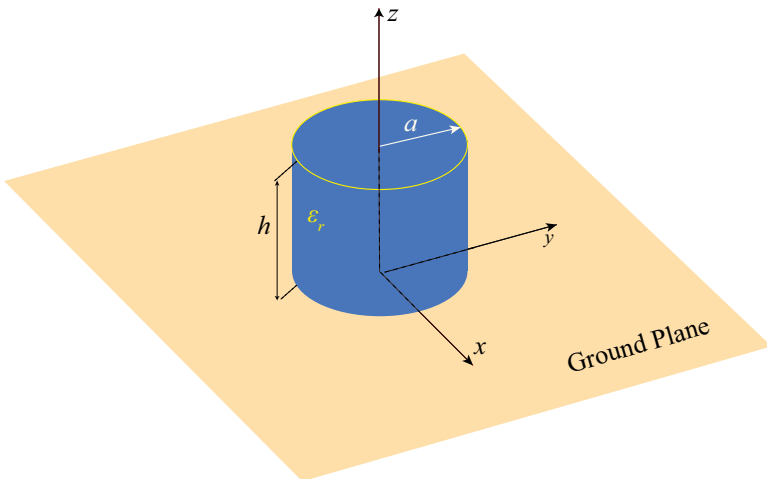

Figure 2.1: The fabricated antenna prototype

The cylindrical shape offers one more degree of design freedom than the hemispherical shape and it is also easier to fabricate. Unlike the hemispherical DRAs, there is no exact solution for the fields within a cylindrical DRA. However, the field can be approximated from the solution for an infinite dielectric rod. For such a dielectric rod, the field can be calculated by solving the Helmholtz equation in cylindrical coordinate system:

$$\frac{1}{\rho}\frac{\partial}{\partial\rho}\left(\rho\frac{\partial\psi}{\partial\rho}\right)+\frac{1}{\rho^2}\frac{\partial^2\psi}{\partial\phi^2}+\frac{\partial^2\psi}{\partial z^2}+k_0^2\psi=0. \tag{2.1}$$

Following the method of separation of variables, we seek for a solution of the form

$$\psi = R(\rho)\Phi(\phi)Z(z). \tag{2.2}$$

Substituting (2.2) in (2.1) we can form a solution to the Helmholtz equation (2.1) as

$$\psi_{k_\rho,n,\beta} = F_n(k_\rho\rho)e^{-\mathrm{j}n\phi}e^{-\mathrm{j}\beta z}, \tag{2.3}$$

where $\beta^2 - k_\rho^2 = k_0^2$, n is a non-negative integer and F_n denotes the solutions of Bessel equation of order n that commonly are [38]

$$F_n(k_\rho\rho) \sim J_n(k_\rho\rho), N_n(k_\rho\rho), H_n^{(1)}(k_\rho\rho), H_n^{(2)}(k_\rho\rho); \tag{2.4}$$

Here $J_n(k_\rho\rho)$ is the Bessel function of the first kind, $N_n(k_\rho\rho)$ is the Bessel function of the second kind, $H_n^{(1)}(k_\rho\rho)$ is the Hankel function of the first kind and $H_n^{(2)}(k_\rho\rho)$ is the Hankel function of the second kind.

The electric and magnetic fields can then be expressed in terms of the scalar function ψ as [38]

$$\mathbf{E} = \frac{1}{\mathrm{j}\omega\varepsilon}\nabla\left(\nabla\cdot(\hat{\mathbf{a}}_z\psi)\right) - \mathrm{j}\omega\mu(\hat{\mathbf{a}}_z\psi) - \nabla\times\hat{\mathbf{a}}_z\psi \tag{2.5}$$

$$\mathbf{H} = \frac{1}{\mathrm{j}\omega\mu}\nabla\left(\nabla\cdot(\hat{\mathbf{a}}_z\psi)\right) - \mathrm{j}\omega\varepsilon(\hat{\mathbf{a}}_z\psi) + \nabla\times\hat{\mathbf{a}}_z\psi \tag{2.6}$$

where ε is the permittivity, μ is the permeability, ω is the angular frequency, $\mathrm{j} = \sqrt{-1}$ and $\hat{\mathbf{a}}_z$ is the unit vector in the $z-$direction.

For a dielectric rod of radius a, the appropriate Bessel functions to use in the region $\rho < a$ is J_n, which represents oscillatory radial standing waves in a cylindrical coordinate system. Since this region contains the origin and the solution needs to be finite everywhere in the region, N_n is excluded from the solution. For the region

$\rho < a$, the fields are expressed by

$$E_z^1 = A_n J_n(k_{\rho d}\rho) e^{-\mathrm{j}n\phi} e^{-\mathrm{j}\beta z} \tag{2.7a}$$

$$E_\rho^1 = \left(-\frac{\mathrm{j}\beta}{k_{\rho d}} A_n J_n'(k_{\rho d}\rho) - \frac{n\omega\mu_0}{k_{\rho d}^2\rho} B_n J_n(k_{\rho d}\rho) \right) e^{-\mathrm{j}n\phi} e^{-\mathrm{j}\beta z} \tag{2.7b}$$

$$E_\phi^1 = \left(-\frac{n\beta}{k_{\rho d}^2\rho} A_n J_n(k_{\rho d}\rho) + \frac{\mathrm{j}\omega\mu_0}{k_{\rho d}} B_n J_n'(k_{\rho d}\rho) \right) e^{-\mathrm{j}n\phi} e^{-\mathrm{j}\beta z} \tag{2.7c}$$

$$H_z^1 = B_n J_n(k_{\rho d}\rho) e^{-\mathrm{j}n\phi} e^{-\mathrm{j}\beta z} \tag{2.7d}$$

$$H_\rho^1 = \left(\frac{n\omega\varepsilon}{k_{\rho d}^2\rho} A_n J_n(k_{\rho d}\rho) - \frac{\mathrm{j}\beta}{k_{\rho d}} B_n J_n'(k_{\rho d}\rho) \right) e^{-\mathrm{j}n\phi} e^{-\mathrm{j}\beta z} \tag{2.7e}$$

$$H_\phi^1 = \left(-\frac{\mathrm{j}\omega\varepsilon}{k_{\rho d}} A_n J_n'(k_{\rho d}\rho) - \frac{n\beta}{k_{\rho d}^2\rho} B_n J_n(k_{\rho d}\rho) \right) e^{-\mathrm{j}n\phi} e^{-\mathrm{j}\beta z} \tag{2.7f}$$

where A_n and B_n are amplitude constants.

For the region $\rho > a$, the solution should represent radial propagating cylindrical waves. Hence, using the $e^{j\omega t}$ time convention, the Hankel function of the second kind is appropriate for the solution in this region. It is expected that the dielectric rod supports slow waves. If slow waves exist, the modulus β is greater than k_0 and the argument of the Hankel function solution for this region would be imaginary (see (2.9)). For more convenience, the Hankel function with imaginary argument is replaced with the modified Bessel function of the second kind, K_n, to get rid of the imaginary argument. The field components in this region are then written as

$$E_z^2 = C_n K_n(k_\rho\rho) e^{-\mathrm{j}n\phi} e^{-\mathrm{j}\beta z} \tag{2.8a}$$

$$E_\rho^2 = \left(\frac{\mathrm{j}\beta}{k_\rho} C_n K_n'(k_\rho\rho) + \frac{n\omega\mu_0}{k_\rho^2\rho} D_n K_n(k_\rho\rho) \right) e^{-\mathrm{j}n\phi} e^{-\mathrm{j}\beta z} \tag{2.8b}$$

$$E_\phi^2 = \left(\frac{n\beta}{k_\rho^2\rho} C_n K_n(k_\rho\rho) - \frac{\mathrm{j}\omega\mu_0}{k_\rho} D_n K_n'(k_\rho\rho) \right) e^{-\mathrm{j}n\phi} e^{-\mathrm{j}\beta z} \tag{2.8c}$$

$$H_z^2 = D_n K_n(k_\rho\rho) e^{-\mathrm{j}n\phi} e^{-\mathrm{j}\beta z} \tag{2.8d}$$

$$H_\rho^2 = \left(-\frac{n\omega\varepsilon_0}{k_\rho^2\rho} C_n K_n(k_\rho\rho) + \frac{\mathrm{j}\beta}{k_\rho} D_n K_n'(k_\rho\rho) \right) e^{-\mathrm{j}n\phi} e^{-\mathrm{j}\beta z} \tag{2.8e}$$

$$H_\phi^2 = \left(\frac{\mathrm{j}\omega\varepsilon_0}{k_\rho} C_n K_n'(k_\rho\rho) + \frac{n\beta}{k_\rho^2\rho} D_n K_n(k_\rho\rho) \right) e^{-\mathrm{j}n\phi} e^{-\mathrm{j}\beta z} \tag{2.8f}$$

where

$$\beta^2 = k_0^2 + k_\rho^2 = \varepsilon_r k_0^2 - k_{\rho d}^2, \tag{2.9}$$

and C_n and D_n are amplitude constants.

In order to fulfill the required boundary condition at the interface, the axial propagation constants for the two regions should be equal. It can be observed that the radiating waves in the presence of a dielectric rod are surface waves. The radial variation of the fields outside the wall are cylindrical decaying functions. This means that the waves are bound to the dielectric surface of the rod. For small-diameter rods, the fields extend for a considerable distance from the surface. In this case the waves are said to be loosely bound to the dielectric surface. As the radius increases, the fields are confined closer to the dielectric surface and the waves are said to be tightly confined to the dielectric surface [39, 40].

Similar to other types of waveguides, the modes in dielectric guides are categorized into TE, TM and hybrid (HE or EH) modes. A pure TM or TE mode exists when the fields are angularly independent. All modes that exhibit angular dependency are combination of a TM and a TE mode. Such a combination is called a hybrid HE or EH mode, depending on whether the TE or TM mode predominates. All of these modes have a cutoff frequency such that, below some minimum value of the electrical radius (a/λ) cannot propagate without attenuation. There is however one exception, the HE_{11} mode, which does not have any cutoff frequency. Since this mode has a zero cutoff, it is referred to as the dominant mode. This mode is widely used in the directional radiators and is usually known as dipole mode [9, 40–45].

The fields within a dielectric resonator are commonly estimated from the field in its corresponding dielectric rod. In this approach, a perfect magnetic conductor (PMC) condition is assumed at all of the dielectric-air interfaces. The modes in cylindrical dielectric resonators are similar to those of cylindrical dielectric rods [9]. They are also divided into three distinct types: TE, TM and hybrid modes. The radial and angular variation of these modes are the same as their namesake for a dielectric rod. However, the z dependence is replaced with 'sin' and 'cos' functions representing the oscillating standing waves in the z-direction. Furthermore, since a dielectric resonator is a three dimensional structure, each mode in a dielectric resonator is distinguished with three indices.

The modes that are most commonly used for radiating application in cylindrical DRAs are $TE_{01\delta}$, $TM_{01\delta}$, and $HE_{11\delta}$ [36, 37]. For $TE_{01\delta}$, the approximated fields inside a cylindrical dielectric resonator are determined by applying PMC boundary condition at the boundaries of the dielectric resonator and setting to zero the non-transverse component of the E-field, ($A_n = 0$) in Equations (2.7). The variation of the $TE_{01\delta}$ fields inside the DRA can then be expressed by

$$E_z = E_\rho = H_\phi = 0 \tag{2.10a}$$

$$E_\phi \propto J_0'(\chi_{01}\rho/a)\sin(\beta z) \tag{2.10b}$$

$$H_z \propto J_0(\chi_{01}\rho/a)\sin(\beta z) \tag{2.10c}$$

$$H_\rho \propto J_0'(\chi_{01}\rho/a)\cos(\beta z) \tag{2.10d}$$

where χ_{01} is the first zero of the zero order Bessel function of the first kind and $\beta = \pi/2h$.

The fields for $TM_{01\delta}$ can be found by interchanging the electric and magnetic fields in (2.10a). For the $HE_{11\delta}$ mode, the E-filed is predominant, and hence the H-field can be approximately ignored as compared to the E-field. The estimated field components for this mode are then

$$E_z \propto J_1(\chi'_{11}\rho/a)\cos(\beta z)\begin{cases}\cos\phi\\ \sin\phi\end{cases} \tag{2.11a}$$

$$E_\rho \propto J'_1(\chi'_{11}\rho/a)\sin(\beta z)\begin{cases}\cos\phi\\ \sin\phi\end{cases} \tag{2.11b}$$

$$E_\phi \propto \frac{J_1(\chi'_{01}\rho/a)}{\rho}\sin(\beta z)\begin{cases}\sin\phi\\ \cos\phi\end{cases} \tag{2.11c}$$

$$H_z \approx 0 \tag{2.11d}$$

$$H_\rho \propto \frac{J_1(\chi'_{11}\rho/a)}{\rho}\cos(\beta z)\begin{cases}\sin\phi\\ \cos\phi\end{cases} \tag{2.11e}$$

$$H_\phi \propto J'_1(\chi'_{11}\rho/a)\cos(\beta z)\begin{cases}\cos\phi\\ \sin\phi\end{cases} \tag{2.11f}$$

where χ'_{11} is the first solution to $J'_1(x) = 0$ and $\beta = \pi/2h$.

The exponential term for ϕ variation in (2.7) is here replaced by $\sin\phi$ and $\cos\phi$, which each represents a $HE_{11\delta}$ mode and are in phase quadrature with respect to each other. The choice of sin or cos depends on the location of the feed.

2.3 Coupling to DRAs

For most practical antenna applications, the electromagnetic power must flow into the DRA from one or more ports. The type of the port and its location relative to the DRA govern the mode that will be excited. This knowledge also helps to predict how efficiently the port couples the power into the DRA. A representation of the approximate distribution of the fields within cylindrical DRAs provided in Section 2.2 gives a useful insight for the excitation of this type of DRAs.

The sources that couple to the DRA, can be typically modeled as either electric or magnetic current. Base on this model the amount of coupling, ξ, between the source and the fields within the DRA can be determined by utilizing the reciprocity theorem with appropriate boundary conditions [37]. For an electric current source $\mathbf{J}_s$, the coupling coefficient is proportional to

$$\xi \propto \int_V (\mathbf{E}_{\mathrm{DRA}}.\mathbf{J}_s)dV, \tag{2.12}$$

and for the magnetic current source $\mathbf{M}_s$

$$\xi \propto \int_V (\mathbf{H}_{\mathrm{DRA}}.\mathbf{M}_s)dV, \tag{2.13}$$

where V is the volume occupied by the source and $\mathbf{E}_{\mathrm{DRA}}$ and $\mathbf{H}_{\mathrm{DRA}}$ are the electric and the magnetic field within the DRA respectively.

According to equation (2.12), it can be stated that for an electric current source, such as a dipole, in order to achieve a strong coupling to the DRA the source should be placed in the area of intensive electric field within the DRA. The same considerations exist for the magnetic current source like slots that should be placed at the location of a strong magnetic field for efficient coupling. It should be noted that the power transference provides just a necessary, but not a sufficient, condition for the antenna to function properly. Other concerns such as the feed impedance and loading effects of the feed, should also be considered in the antenna design process.

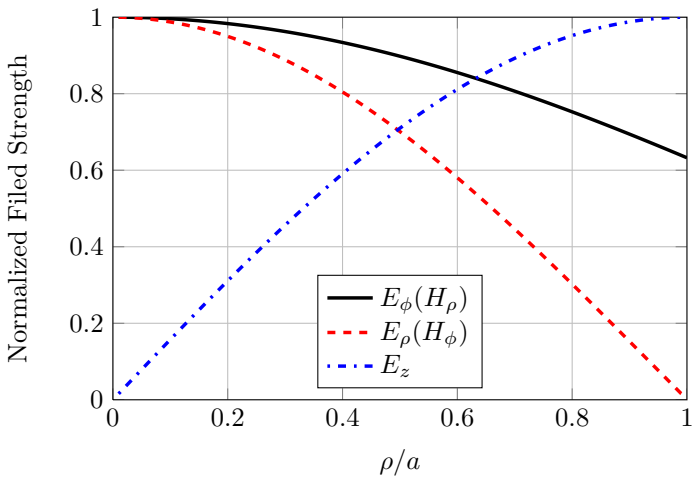

Figure 2.2: Normalized field strength for $\mathrm{HE}_{11\delta}$ modes in a cylindrical DRA.

The normalized field strength for the $\mathrm{HE}_{11\delta}$ modes in a cylindrical DRA are plotted in Fig. 2.2. It can be observed that the electric field in the z-direction is at a maximum at the outer surface of a cylindrical DRA for the $\mathrm{HE}_{11\delta}$ mode. Therefore, this mode can be excited by a vertical dipole or strip along the z-direction located adjacent or slightly into the side wall of the cylindrical DRA [28, 46].

According to the curves plotted in Fig. 2.2, the ϕ-component of the magnetic field is maximal at the center of a cylindrical DRA. A proper sized slot located at the center of a cylindrical DRA can therefore be used to excite the $\mathrm{HE}_{11\delta}$ mode in the DRA [47].

The inspiration for the antenna introduced in this thesis first arrived after an investigation of the field distribution in a cylindrical DRA shown in Fig. 2.2. It can be observed that for a cylindrical DRA, the $z-$ component of the electric field due to the $HE_{11\delta}$ mode has its maximum on the outer surface. Furthermore, the $\phi-$ component of the electric field in this mode also has a relatively high value on the outer surface. Hence, if an electric current source containing both $z-$ and $\phi-$ components is located at this place, a strong coupling to the DRA is expected. Such a current can be produced by an external conducting helix that is wound around the DRA. A helix carrying a current that at each point has both $z-$component and $\phi-$ components.

Chapter 3

The Helix

3.1 Introduction

A helix is a type of smooth three-dimensional curve with the property that the tangent line at any point makes a constant angle with a fixed line called the axis. Fig. 3.1(a) shows a typical helix. Viewed end-on, a helix projects to a circle. The diameter of this circle is called the helix diameter. The pitch or turn spacing of a helix, S, is the height of one complete turn of the helix, measured parallel to its axis. If one turn of a circular helix is unrolled on a flat plane, the relation between the helix diameter, pitch and length of one turn can be illustrated as in Fig. 3.1(b). The angle α is the helix pitch angle.

A realization of a helical curve can be formed by a conducting wire. A conducting helix is a periodic slow wave structure. This is a practical device in the electromagnetic engineering field. It is used in low, medium and high power traveling wave tubes [48–50], and in low-power backward-wave oscillators [51]. The helix is particularly used in radiating structures. It is used as a highly directive broad band circularly polarized antenna [52], or as a circularly polarized feed for other type of antennas [53–55].

3.2 Analysis of the Helix

The Helmholtz equation is not separable in a helical coordinate system [39]. Consequently, the solution for an electromagnetic wave propagating along a helix is usually achieved by the aid of some approximations. Two approximate models that are mostly used to analyze the helix are to replace the actual helix with a sheath helix or an infinitely thin conducting tape [50, 56, 57]. The sheath helix is the simplest model for the actual helix. This is a cylindrical tube which is assumed to have perfect conductivity in the direction of the original winding and zero conductivity in the bi-normal direction to the direction of winding. The analysis of a sheath helix is based on the general expansion of fields in cylindrical coordinates in regions

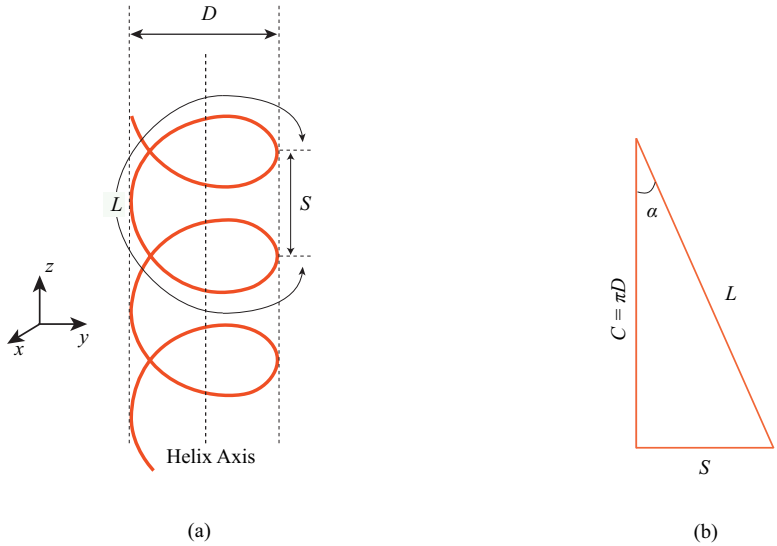

Figure 3.1: (a)A typical helix curve and it's parameters (b) The relation between circumference, C, spacing, S, turn length, L and pitch angle, α in a helix.

inside and outside the helix, and then to impose the appropriate boundary conditions for the interface of the two regions based on the assumed current density on the sheath helix surface. [39, 50]

The tape helix is a more representative physical model of the wire helix [56]. The essential steps in the analysis of this structure are to first write the field expansion in cylindrical coordinates for the inside and outside regions of the helix, and then to determine the amplitude coefficients in terms of an assumed electric field in the gap, or in terms of an assumed current on the tape. The Floquet theorem is also used to adjust the priorities of the solution with the physical peridiymis of the actual helix [50, 56].

A helix can operate in different distinct modes. The mode of operation is governed by the dimensions of the helix relative to the wavelength. The areas corresponding to each mode of operation, as a function of dimensions of the helix , are illustrated in Fig. 3.2. The most practical mode of operation, when the helix is used for radiation applications, is the axial mode. Axial-mode helixes are used as frequency shifters, polarizers, feeds for antennas, and radiating elements.

One of the methods for the analysis of the radiation characteristics of a helix, is to consider it as a periodic array structure with a period equal to the turn spacing. The array is then assumed to be fed by a wave traveling along the array axis via a guiding structure, which may, for example, be the helix itself or a dielectric rod or a tube supporting the helix. In the case of axial-mode operation, the radiation pattern

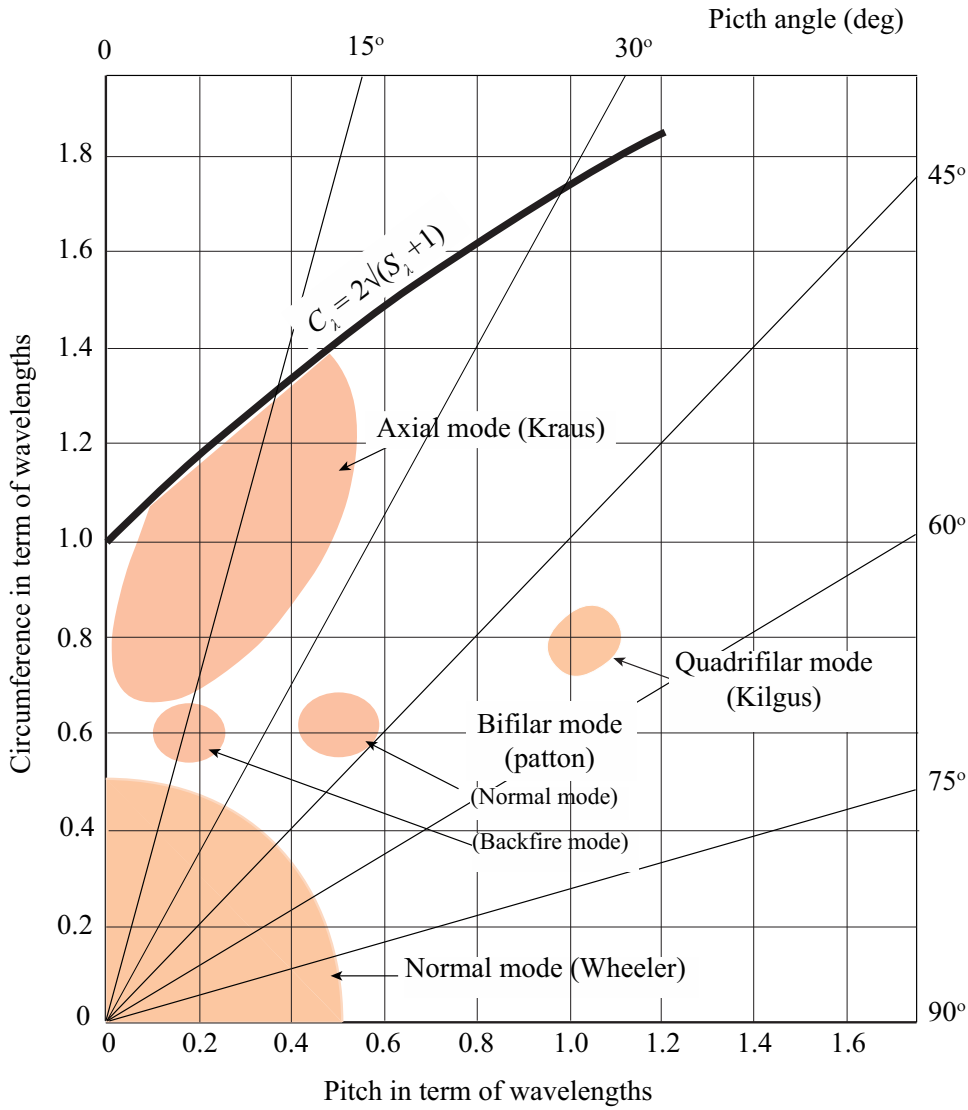

Figure 3.2: The Helix chart (reproduced from [52] under Mc-Graw Hill permission licence NO. ALI32138).

of the antenna can be well approximated with the Hansen–Woodyard increased directivity condition for linear phase arrays [52].

Hansen–Woodyard Increased Directivity Condition

Let us consider a linear, equally spaced array of N identical point source antenna elements as shown in Fig. 3.3. If all of the elements have the identical magnitude with a constant phase progression, δ, the array factor of this linear antenna array is given by

$$\mathrm{AF} = \sum_{n=1}^{N} \exp[\mathrm{j}(n-1)(k_0 d\cos\theta + \delta)], \tag{3.1}$$

where k_0 is the wave number in free space. With some mathematical manipulation, the array factor can be written as [58]

$$\mathrm{AF} \approx \frac{\sin[\frac{N}{2}(k_0 d\cos\theta + \delta)]}{\frac{N}{2}(k_0 d\cos\theta + \delta)}. \tag{3.2}$$

The first maximum of the array factor in (3.2) occurs when the argument of the sin function becomes zero

$$k_0 d\cos\theta + \delta = 0. \tag{3.3}$$

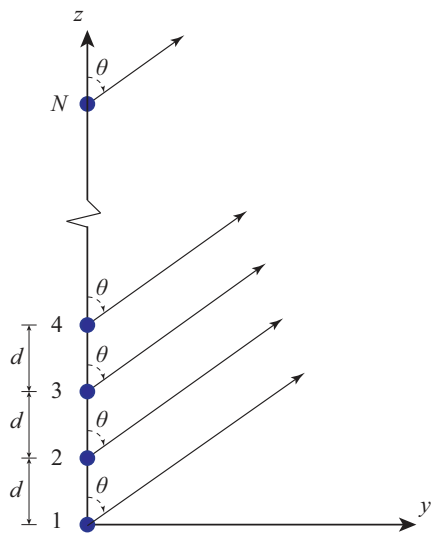

Figure 3.3: $N-$element array of point source along the $z-$axis.

Hence, in order to direct the maximum radiation along the axis of the array (end-fire), (3.3) should be hold for $\theta = 0$ or $\theta = \pi$. This condition is known as the *ordinary end-fire* condition for uniform linear arrays.

For the helix as an array of elements, the element spacing is equal to the helix pitch. Considering the helix as a surface wave structure, the phase difference between the two adjacent elements would be equal to

$$\delta = -\beta s, \tag{3.4}$$

where β is the phase constant of the cylindrical surface wave traveling along the axis of the helix and s is the helix pitch.

Imposing (3.4) in (3.3) for end-fire radiation, with $s = d$, gives $k_0 = \beta$, which is a contradiction due to the slow wave nature of the helix. However, the axial mode end-fire radiation of the helix can be well simulated with a linear array under the Hansen–Woodyard condition [52]. When the element spacing is small ($d \ll \lambda$), Hansen and Woodyard [59] proposed a condition for the required phase shift between the adjacent elements to enhance the directivity of a uniform array with end-fire radiation. This phase shift, to have the maximum radiation intensity at $\theta = 0$ or $\theta = \pi$ is given by

$$\delta \approx \pm(k_0 d + \pi/N). \tag{3.5}$$

This requirement is known as the Hansen–Woodyard condition for end-fire radiation and leads to a larger directivity than the ordinary end-fire condition for linear arrays.

Chapter 4

Phase Velocity in Dielectric Rods and Tubes

4.1 Introduction

It was mentioned in Section 2.1 that the dielectric tubes and rods [1] are widely used in communication as wave guides and radiators. They are also used for supporting helical antennas [52]. As described in Chapter 3, one of the methods used to analyze the characteristics of a helical antenna is to consider it as an array of conductors. These conductors are fed by a traveling wave in the direction of the helix axis. It was also mentioned that the radiation pattern of a helix operating in the axial mode has a good agreement with the radiation pattern of an end-fire linear array under the Hansen–Woodyard condition [52]. The important factor in this analysis is the set of characteristics of the traveling wave that feed the array elements, and, in particular, the phase velocity of this feeding wave.

In this thesis, cylindrical and ring shape (hollow cylinder) dielectric resonators are loaded to the helix as supporters. In the case in which a helix is supported by a circular cross section dielectric resonator, or from another perspective, a dielectric resonator that is excited by a helix, the dielectric resonator height is usually shorter than that of the helix. In this case, the feeding wave is the surface wave traveling in the direction of the axis of the dielectric resonator. The exact analytical solution for a cylindrical and ring shape dielectric resonator does not exist. However, the dielectric resonator can be considered as a dielectric rod transmission line that is terminated. The termination of a transmission does not significantly affect its characteristics. Hence, the solution for infinitely long dielectric rods and tubes can be used to estimate the phase velocity of a traveling surface wave along the cylindrical and ring dielectric resonators, respectively.

[1] In this thesis dielectric rod refers to an infinitely long circular cross section cylindrical dielectric rod. Correspondingly, dielectric tube denotes an infinite circular cross section cylindrical shell.

In this chapter, the dielectric rod and tube are analytically investigated. The helixes do not have angular symmetry. Hence, TM or TE surface wave modes do not exist in the cylindrical dielectric supporter of the helix. In this case, the hybrid modes that are a combination of TM or TE, can exist. All of these hybrid modes exhibit a cutoff frequency with the exception of the HE_{11} modes that have no cutoff frequency (zero cutoff). These modes are the dominant modes in the dielectric rods and tubes and are widely used for radiation applications [39, 45]. In the following two sections, the phase velocity of the HE_{11} surface wave modes in a dielectric rod and tube are determined. These phase velocities are compared for different values of the dielectric constant in a dielectric rod and for different values of the wall thickness for the dielectric tube.

4.2 Dielectric Rods

The field component expansions for the hybrid mode for a circular dielectric rod was expressed in (2.7) and (2.8) for inner and outer region respectively. The coefficient A_n, B_n, C_n, and D_n are related to each other by imposing the boundary conditions at $\rho = a$, where a is the radius of the rod. The boundary conditions at $\rho = a$ require continuity of electric and magnetic field component of

$$E_z^1(\rho = a, \phi, z) = E_z^2(\rho = a, \phi, z) \tag{4.1}$$
$$E_\phi^1(\rho = a, \phi, z) = E_\phi^2(\rho = a, \phi, z) \tag{4.2}$$
$$H_z^1(\rho = a, \phi, z) = H_z^2(\rho = a, \phi, z)$$
$$H_\phi^1(\rho = a, \phi, z) = H_\phi^2(\rho = a, \phi, z)$$

Imposing the boundary conditions and writing the resulting equations in a matrix form gives

$$\begin{bmatrix} J_n(k_{\rho d}a) & 0 & -K_n(k_\rho a) & 0 \\ -\frac{n\beta}{k_{\rho d}^2 \rho} J_n(k_{\rho d}a) & \frac{\mathrm{j}\omega\mu_0}{k_{\rho d}} J_n'(k_{\rho d}a) & -\frac{n\beta}{k_\rho^2 a} K_n(k_\rho a) & \frac{\mathrm{j}\omega\mu_0}{k_\rho} K_n'(k_\rho a) \\ 0 & J_n(k_{\rho d}a) & 0 & -K_n(k_\rho a) \\ \frac{\mathrm{j}\omega\varepsilon}{k_{\rho d}} J_n'(k_{\rho d}a) & \frac{n\beta}{k_{\rho d}^2 a} B_n J_n(k_{\rho d}a) & \frac{\mathrm{j}\omega\varepsilon_0}{k_\rho} K_n'(k_\rho a) & \frac{n\beta}{k_\rho^2 a} K_n(k_\rho a) \end{bmatrix} \begin{bmatrix} A_n \\ B_n \\ C_n \\ D_n \end{bmatrix} = \mathbf{0} \tag{4.3}$$

Equation (4.3) has a nontrivial solution for the coefficients A_n, B_n, C_n, and D_n, provided that the determinant of the square matrix vanishes. Applying this condition to the square matrix in (4.3) and with some mathematical manipulations we obtain the eigenvalue equation of a dielectric rod of relative permittivity ε_r and radius a as [39]

$$\left[\frac{\varepsilon_r J_n'(u_1)}{u_1 J_n(u_1)} + \frac{K_n'(u_2)}{u_2 K_n(u_2)}\right]\left[\frac{J_n'(u_1)}{u_1 J_n(u_1)} + \frac{K_n'(u_2)}{u_2 K_n(u_2)}\right] = \left[\frac{n\beta}{k_0}\frac{u_1^2+u_2^2}{u_1^2 u_2^2}\right]^2, \qquad (4.4)$$

where $u_1 = k_{\rho d}a, u_2 = k_\rho a$ and $\beta^2 = k_0^2 + k_\rho^2 = \varepsilon_r k_0^2 - k_{\rho d}^2$.

Numerical Solution

Equation (4.4) is solved in Matlab for u_1 and u_2. It is known that u_1 and u_2 are related together as

$$u_1^2 + u_2^2 = (\varepsilon_r - 1)k_0^2 a^2 = R^2, \qquad (4.5)$$

where R is a constant that is dependent on the relative permittivity and radius of the dielectric rod and the free space wavenumber, k_0. Equation (4.5) can be reformulated as

$$u_1 = R\sin y \qquad u_2 = R\cos y \qquad (4.6)$$

Substituting (4.6) in (4.4), gives an equation with one unknown, y. The resulting equation is solved using `fminbnd` command in Matlab. The relative phase velocity in terms of y is given by

$$\frac{v}{c} = \frac{k_0}{\beta} = \frac{1}{\sqrt{\sin^2 y + \varepsilon_r \cos^2 y}}. \qquad (4.7)$$

The numerical solution for the relative axial phase velocity (phase velocity along the axis of the cylinder) in dielectric rods with three different values of the dielectric constant, as a function of the normalized circumference of the rod, is plotted in Fig. 4.1. It can be seen that for small values of the radius the axial phase velocity in a dielectric rod is close to the velocity of light, c. For very large value of the radius it converges to the value $c/\sqrt{\varepsilon_r}$. Furthermore, the slope of the curve is steeper for a rod with a greater dielectric constant. In other words, for a given value of the radius, the relative phase velocity is smaller for rods with higher dielectric constants.

The electric field intensity for all components of the HE_{11} mode as well as the magnitude of the total electric field of this mode in a dielectric rod are illustrated in Fig. 4.2. The dielectric constant of the rod is $\varepsilon_r = 10$. The fields are plotted for $k_0 a = 0.75$. Based on the solution for the phase velocity for the case $\varepsilon_r = 10$ presented in Fig. 4.1, for $k_0 a = 0.75$ we have $k_0/\beta = 0.616$. The fields outside the rod are shown for a distance equal to the radius of the rod from the outer surface of the rod. It can be observed that a good agreement exists between the approximated field distribution of the $HE_{11\delta}$ in a cylindrical DRA that was shown in Fig. 2.2 and the HE_{11} mode in a dielectric rod. The ϕ-component of the electric field is maximal at the center and slowly decreases up to the surface of the rod.

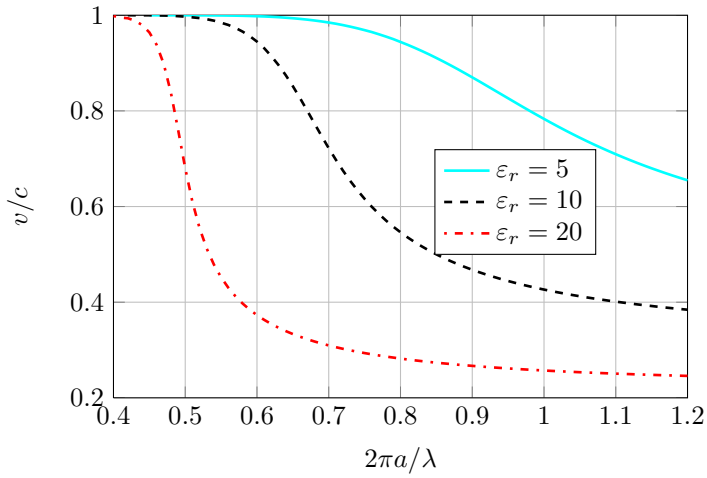

Figure 4.1: Normalized phase velocity of the HE_{11} surface eave mode in dielectric rods for three different dielectric constant as a function of the normalized circumference of the rod.

This reduction is continued outside of the rod with a faster rate than it was in the inside region. The maximum radial component is in the outer region of the rod. It is also high at the center and rapidly diminishes to low values at the inner surface of the rod. The z-component vanishes at the center. This increases to its maximum at the inner surface and slowly decreases with distance beyond the surface in the outside region. The intensity of the total electric field is shown in Fig. 4.2(d). It is shown that the electric filed is bound to the surface of the rod in the outer region. By increasing the frequency, the field will be more tightly bound to the surface.

4.3 Dielectric Tubes

The same type of analysis as was done for dielectric rods, can be utilized for dielectric tubes. In the case of dielectric tube the analysis is more difficult than the case of the rod as there are two boundaries to be considered, the inner and outer tube surfaces, and also additional parameter, the tube wall thickness $b-a$, see Fig. 4.3. The dielectric tube separates the space into three regions. These regions are illustrated in Fig. 4.3.

In the region 1, the free space medium inside the tube when $\rho \leq a$, the solution for fields must represent cylindrical standing waves with oscillatory behavior. The cylindrical functions that represent this kind of radial variations of the fields are J_n, the Bessel function of the first kind, and N_n, the Bessel function of the second kind [38]. However, since the region contains the origin, N_n should be excluded

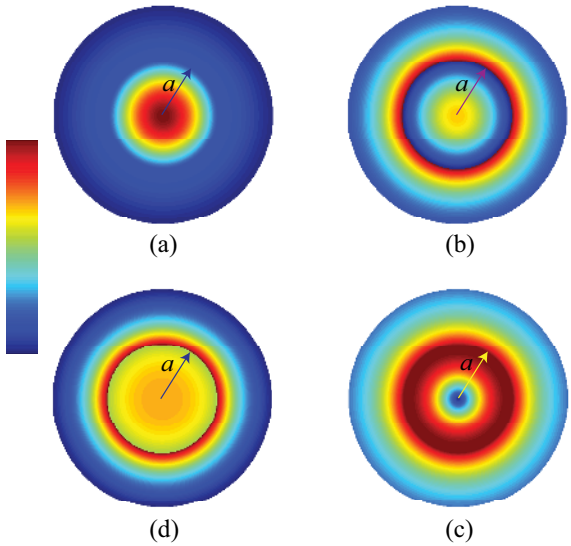

Figure 4.2: The intensity of the electric field components of the HE_{11} mode with $e^{-j\phi}$ azimuthal variation, inside and outside of a dielectric rod of permittivity $\varepsilon_r = 10$ on a cross sectional transverse plane. (a) $|E_\phi|$, (b) $|E_\rho|$, (c) $|E_z|$ and $|\mathbf{E}|$. The field are plotted for $k_0 a = 0.75$ that leads to $k_0/\beta = 0.616$.

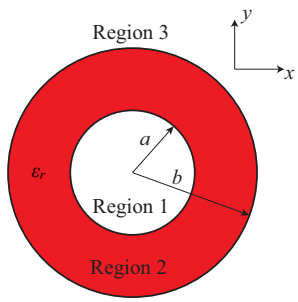

Figure 4.3: The cross section of a dielectric tube.

from the solution. Furthermore, in the tube case, the Bessel function of the first kind J_n with imaginary argument is converted to the modified Bessel function of the first kind, I_n. The fields components in the region 1, $\rho \leq a$, can then be expressed as

$$E_z^1 = A_n I_n(k_\rho \rho) e^{-\mathrm{j}n\phi} e^{-\mathrm{j}\beta z} \tag{4.8a}$$

$$E_\rho^1 = \left(\frac{\mathrm{j}\beta}{k_\rho} A_n I_n'(k_\rho \rho) + \frac{n\omega\mu_0}{k_\rho^2 \rho} B_n I_n(k_\rho \rho) \right) e^{-\mathrm{j}n\phi} e^{-\mathrm{j}\beta z} \tag{4.8b}$$

$$E_\phi^1 = \left(\frac{n\beta}{k_\rho^2 \rho} A_n I_n(k_\rho \rho) - \frac{\mathrm{j}\omega\mu_0}{k_\rho} B_n I_n'(k_\rho \rho) \right) e^{-\mathrm{j}n\phi} e^{-\mathrm{j}\beta z} \tag{4.8c}$$

$$H_z^1 = B_n I_n(k_\rho \rho) e^{-\mathrm{j}n\phi} e^{-\mathrm{j}\beta z} \tag{4.8d}$$

$$H_\rho^1 = \left(-\frac{n\omega\varepsilon_0}{k_\rho^2 \rho} A_n I_n(k_\rho \rho) + \frac{\mathrm{j}\beta}{k_\rho} B_n I_n'(k_\rho \rho) \right) e^{-\mathrm{j}n\phi} e^{-\mathrm{j}\beta z} \tag{4.8e}$$

$$H_\phi^1 = \left(\frac{\mathrm{j}\omega\varepsilon_0}{k_\rho} A_n I_n'(k_\rho \rho) + \frac{n\beta}{k_\rho^2 \rho} B_n I_n(k_\rho \rho) \right) e^{-\mathrm{j}n\phi} e^{-\mathrm{j}\beta z} \tag{4.8f}$$

Region 2 is the dielectric medium inside the tube wall, $a \leq \rho \leq b$. The solutions in this region should also represent standing wave with oscillatory behavior. However, this region does not contain the origin and the Bessel function of the second kind, N_n, should be included in the solution:

$$E_z^2 = \left[L_n J_n(k_{\rho d}\rho) + M_n N_n(k_{\rho d}\rho) \right] e^{-\mathrm{j}n\phi} e^{-\mathrm{j}\beta z} \tag{4.9a}$$

$$\begin{aligned} E_\rho^2 = \Big(& -\frac{\mathrm{j}\beta}{k_{\rho d}} \left[L_n J_n'(k_{\rho d}\rho) + M_n N_n'(k_{\rho d}\rho) \right] \\ & - \frac{n\omega\mu_0}{k_{\rho d}^2 \rho} \left[P_n J_n(k_{\rho d}\rho) + Q_n N_n(k_{\rho d}\rho) \right] \Big) e^{-\mathrm{j}n\phi} e^{-\mathrm{j}\beta z} \end{aligned} \tag{4.9b}$$

$$\begin{aligned} E_\phi^2 = \Big(& -\frac{n\beta}{k_{\rho d}^2 \rho} \left[L_n J_n(k_{\rho d}\rho) + M_n N_n(k_{\rho d}\rho) \right] \\ & + \frac{\mathrm{j}\omega\mu_0}{k_{\rho d}} \left[P_n J_n'(k_{\rho d}\rho) + Q_n N_n'(k_{\rho d}\rho) \right] \Big) e^{-\mathrm{j}n\phi} e^{-\mathrm{j}\beta z} \end{aligned} \tag{4.9c}$$

$$H_z^2 = \left[P_n J_n(k_{\rho d}\rho) + Q_n N_n(k_{\rho d}\rho) \right] e^{-\mathrm{j}n\phi} e^{-\mathrm{j}\beta z} \tag{4.9d}$$

$$\begin{aligned} H_\rho^2 = \Big(& \frac{n\omega\varepsilon}{k_{\rho d}^2 \rho} \left[L_n J_n(k_{\rho d}\rho) + M_n N_n(k_{\rho d}\rho) \right] \\ & - \frac{\mathrm{j}\beta}{k_{\rho d}} \left[P_n J_n'(k_{\rho d}\rho) + Q_n N_n'(k_{\rho d}\rho) \right] \Big) e^{-\mathrm{j}n\phi} e^{-\mathrm{j}\beta z} \end{aligned} \tag{4.9e}$$

$$\begin{aligned} H_\phi^2 = \Big(& -\frac{\mathrm{j}\omega\varepsilon}{k_{\rho d}} \left[L_n J_n'(k_{\rho d}\rho) + M_n N_n'(k_{\rho d}\rho) \right] \\ & - \frac{n\beta}{k_{\rho d}^2 \rho} \left[P_n J_n(k_{\rho d}\rho) + Q_n N_n(k_{\rho d}\rho) \right] \Big) e^{-\mathrm{j}n\phi} e^{-\mathrm{j}\beta z} \end{aligned} \tag{4.9f}$$

For region 3, the radial variation of the waves are cylindrical traveling waves. Nevertheless, based on a similar argumentation as described for dielectric rods

in Section 2.2, the waves are confined to the outer surface of tube and should represent a decaying behavior. Hankel functions with imaginary arguments or their equivalent, the modified Bessel function of the second kind K_n are appropriate in this region. The fields component are then written as

$$E_z^3 = C_n K_n(k_\rho \rho) e^{-\mathrm{j}n\phi} e^{-\mathrm{j}\beta z} \tag{4.10a}$$

$$E_\rho^3 = \left(\frac{\mathrm{j}\beta}{k_\rho} C_n K_n'(k_\rho \rho) + \frac{n\omega\mu_0}{k_\rho^2 \rho} D_n K_n(k_\rho \rho) \right) e^{-\mathrm{j}n\phi} e^{-\mathrm{j}\beta z} \tag{4.10b}$$

$$E_\phi^3 = \left(\frac{n\beta}{k_\rho^2 \rho} C_n K_n(k_\rho \rho) - \frac{\mathrm{j}\omega\mu_0}{k_\rho} D_n K_n'(k_\rho \rho) \right) e^{-\mathrm{j}n\phi} e^{-\mathrm{j}\beta z} \tag{4.10c}$$

$$H_z^3 = D_n K_n(k_\rho \rho) e^{-\mathrm{j}n\phi} e^{-\mathrm{j}\beta z} \tag{4.10d}$$

$$H_\rho^3 = \left(-\frac{n\omega\varepsilon_0}{k_\rho^2 \rho} C_n K_n(k_\rho \rho) + \frac{\mathrm{j}\beta}{k_\rho} D_n K_n'(k_\rho \rho) \right) e^{-\mathrm{j}n\phi} e^{-\mathrm{j}\beta z} \tag{4.10e}$$

$$H_\phi^3 = \left(\frac{\mathrm{j}\omega\varepsilon_0}{k_\rho} C_n K_n'(k_\rho \rho) + \frac{n\beta}{k_\rho^2 \rho} D_n K_n(k_\rho \rho) \right) e^{-\mathrm{j}n\phi} e^{-\mathrm{j}\beta z} \tag{4.10f}$$

The relation between the constant coefficients, $A_n, B_n, C_n, D_n, L_m, M_n$, can be obtained by applying the boundary condition for continuity of electric and magnetic field components as

$$\begin{aligned}
E_z^1(\rho = a, \phi, z) &= E_z^2(\rho = a, \phi, z) & E_z^2(\rho = b, \phi, z) &= E_z^3(\rho = b, \phi, z) \\
E_\phi^1(\rho = a, \phi, z) &= E_\phi^2(\rho = a, \phi, z) & E_\phi^2(\rho = b, \phi, z) &= E_\phi^3(\rho = b, \phi, z) \\
H_z^1(\rho = a, \phi, z) &= H_z^2(\rho = a, \phi, z) & H_z^2(\rho = b, \phi, z) &= H_z^3(\rho = b, \phi, z) \\
H_\phi^1(\rho = a, \phi, z) &= H_\phi^2(\rho = a, \phi, z) & H_\phi^2(\rho = b, \phi, z) &= H_\phi^3(\rho = b, \phi, z)
\end{aligned} \tag{4.11}$$

Substituting (4.8), (4.9), and (4.10) in (4.11) gives

$$\begin{aligned}
A_n J_n(k_\rho a) &= L_n J_n(k_{\rho d} a) + M_n N_n(k_{\rho d} a) \\
L_n J_n(k_{\rho d} b) + M_n N_n(k_{\rho d} b) &= C_n K_n(k_\rho b) \\
-\frac{n\beta}{k_\rho^2 \rho} A_n J_n(k_\rho a) + \frac{\mathrm{j}\omega\mu_0}{k_\rho} B_n J_n'(k_\rho a) &= -\frac{n\beta}{k_{\rho d}^2 a} \left[L_n J_n(k_{\rho d} a) + M_n N_n(k_{\rho d} a) \right] \\
&\quad + \frac{\mathrm{j}\omega\mu_0}{k_{\rho d}} \left[P_n J_n'(k_{\rho d} a) + Q_n N_n'(k_{\rho d} a) \right] \\
-\frac{n\beta}{k_{\rho d}^2 \rho} \left[L_n J_n(k_{\rho d} b) + M_n N_n(k_{\rho d} b) \right] + \frac{\mathrm{j}\omega\mu_0}{k_{\rho d}} \left[P_n J_n'(k_{\rho d} b) + Q_n N_n'(k_{\rho d} b) \right] & \\
&= \frac{n\beta}{k_\rho^2 \rho} C_n K_n(k_\rho b) - \frac{\mathrm{j}\omega\mu_0}{k_\rho} D_n K_n'(k_\rho b)
\end{aligned}$$

$$
\begin{aligned}
B_n J_n(k_\rho a) &= P_n J_n(k_{\rho d} a) + Q_n N_n(k_{\rho d} a) \\
P_n J_n(k_{\rho d} b) + Q_n N_n(k_{\rho d} b) &= D_n K_n(k_\rho b) \\
-\frac{\mathrm{j}\omega\varepsilon_0}{k_\rho} A_n J_n'(k_\rho a) - \frac{n\beta}{k_\rho^2 \rho} B_n J_n(k_\rho a) &= -\frac{\mathrm{j}\omega\varepsilon}{k_{\rho d}} \left[L_n J_n'(k_{\rho d} a) + M_n N_n'(k_{\rho d} a) \right] \\
&\quad - \frac{n\beta}{k_{\rho d}^2 \rho} \left[P_n J_n(k_{\rho d} a) + Q_n N_n(k_{\rho d} a) \right] \\
-\frac{\mathrm{j}\omega\varepsilon}{k_{\rho d}} \left[L_n J_n'(k_{\rho d} b) + M_n N_n'(k_{\rho d} b) \right] - \frac{n\beta}{k_{\rho d}^2 \rho} \left[P_n J_n(k_{\rho d} b) + Q_n N_n(k_{\rho d} b) \right] & \\
&= \frac{\mathrm{j}\omega\varepsilon_0}{k_\rho} C_n K_n'(k_\rho b) + \frac{n\beta}{k_\rho^2 b} D_n K_n(k_\rho b)
\end{aligned}
\tag{4.12}
$$

Equation (4.12) can be written in a matrix form as $\mathbf{MX} = \mathbf{0}$. The elements of the square matrix $\mathbf{M}$ can then be written as

$$
\begin{array}{ccccc}
J_n(k_\rho a) & 0 & 0 & 0 & \dots \\
0 & 0 & K_n(k_\rho b) & 0 & \\
-\frac{n\beta}{k_\rho^2 a} J_n(k_\rho a) & \frac{\mathrm{j}\omega\mu_0}{k_\rho} B_n J_n'(k_\rho a) & 0 & 0 & \dots \\
0 & 0 & -\frac{n\beta}{k_\rho^2 b} K_n(k_\rho b) & \frac{\mathrm{j}\omega\mu_0}{k_\rho} K_n'(k_\rho b) & \dots \\
0 & J_n(k_\rho a) & 0 & 0 & \dots \\
0 & 0 & 0 & -K_n(k_\rho b) & \dots \\
-\frac{\mathrm{j}\omega\varepsilon_0}{k_\rho} J_n'(k_\rho a) & -\frac{n\beta}{k_\rho^2 a} J_n(k_\rho a) & 0 & 0 & \dots \\
0 & 0 & \frac{\mathrm{j}\omega\varepsilon_0}{k_\rho} K_n'(k_\rho b) & \frac{n\beta}{k_\rho^2 b} K_n(k_\rho b) & \dots
\end{array}
$$

$$
\begin{array}{ccccc}
\dots & -J_n(k_{\rho d} a) & -N_n(k_{\rho d} a) & 0 & 0 \\
\dots & J_n(k_{\rho d} b) & N_n(k_{\rho d} b) & 0 & 0 \\
\dots & \frac{n\beta}{k_{\rho d}^2 a} J_n(k_{\rho d} a) & \frac{n\beta}{k_{\rho d}^2 a} N_n(k_{\rho d} a) & -\frac{\mathrm{j}\omega\mu_0}{k_{\rho d}} J_n'(k_{\rho d} a) & -\frac{\mathrm{j}\omega\mu_0}{k_{\rho d}} N_n'(k_{\rho d} a) \\
\dots & -\frac{n\beta}{k_{\rho d}^2 b} J_n(k_{\rho d} b) & -\frac{n\beta}{k_{\rho d}^2 b} N_n(k_{\rho d} b) & \frac{\mathrm{j}\omega\mu_0}{k_{\rho d}} J_n'(k_{\rho d} b) & \frac{\mathrm{j}\omega\mu_0}{k_{\rho d}} N_n'(k_{\rho d} b) \\
\dots & 0 & 0 & -J_n(k_{\rho d} a) & -N_n(k_{\rho d} a) \\
\dots & 0 & 0 & J_n(k_{\rho d} b) & N_n(k_{\rho d} b) \\
\dots & \frac{\mathrm{j}\omega\varepsilon}{k_{\rho d}} J_n'(k_{\rho d} a) & \frac{\mathrm{j}\omega\varepsilon}{k_{\rho d}} N_n'(k_{\rho d} a) & \frac{n\beta}{k_{\rho d}^2 a} J_n(k_{\rho d} a) & \frac{n\beta}{k_{\rho d}^2 a} N_n(k_{\rho d} a) \\
\dots & \frac{\mathrm{j}\omega\varepsilon}{k_{\rho d}} J_n'(k_{\rho d} b) & \frac{\mathrm{j}\omega\varepsilon}{k_{\rho d}} N_n'(k_{\rho d} b) & \frac{n\beta}{k_{\rho d}^2 b} J_n(k_{\rho d} b) & \frac{n\beta}{k_{\rho d}^2 b} N_n(k_{\rho d} b)
\end{array}
\tag{4.13}
$$

where $\beta^2 = k_0^2 + k_\rho^2 = \varepsilon_r k_0^2 - k_{\rho d}^2$.

The above mentioned equation represent a homogamous linear system of equations. To have a nontrivial solution of such a system, the determinant of the matrix **M** should vanish. Equating the evaluated determinant of **M** to zero gives the characteristic equation of the dielectric tube [45]:

$$\begin{aligned}
&-n^4T^4\left(\Delta_3-\Delta_4\right)^2\\
&-\left(a/b\right)^4\varepsilon_r^2Q^2[\Delta_3\left(\Delta_1-\Delta_9/\varepsilon_r\right)\left(\Delta_8-\Delta_5/\varepsilon_r\right)\\
&-\Delta_4\left(\Delta_7-\Delta_9/\varepsilon_r\right)\left(\Delta_2-\Delta_5/\varepsilon_r\right)]\\
&\quad[\Delta_3(\Delta_1-\Delta_9)(\Delta_8-\Delta_5)-\Delta_4(\Delta_7-\Delta_9)(\Delta_2-\Delta_5)]\\
&-2n^2T^2\varepsilon_rQ(b/a)^2\Delta_3\Delta_4(\Delta_1-\Delta_7)(\Delta_2-\Delta_8)\\
&+n^2T^2\varepsilon_rQ[(\Delta_8\Delta_3-\Delta_2\Delta_4)-\Delta_5(\Delta_3-\Delta_4)]\\
&\quad[(\Delta_8\Delta_3-\Delta_2\Delta_4)-(\Delta_5/\varepsilon_r)(\Delta_3-\Delta_4)]\\
&+n^2T^2\varepsilon_rQ(b/a)^4[(\Delta_1\Delta_3-\Delta_7\Delta_4)-\Delta_9(\Delta_3-\Delta_4)]\\
&\quad[(\Delta_1\Delta_3-\Delta_7\Delta_4)-(\Delta_9/\varepsilon_r)(\Delta_3-\Delta_4)]=0
\end{aligned} \tag{4.14}$$

where

$$\Delta_1=\frac{J_n'(k_{\rho d}a)}{k_{\rho d}aJ_n(k_{\rho d}a)} \qquad \Delta_5=-\frac{K_n'(k_\rho b)}{k_\rho bK_n(k_\rho b)}$$

$$\Delta_2=\frac{J_n'(k_{\rho d}b)}{k_{\rho d}bJ_n(k_{\rho d}b)} \qquad \Delta_7=\frac{N_n'(k_{\rho d}a)}{k_{\rho d}aN_n(k_{\rho d}a)}$$

$$\Delta_3=\frac{J_n'(k_{\rho d}a)}{N_n(k_{\rho d}a)} \qquad \Delta_8=\frac{N_n'(k_{\rho d}b)}{k_{\rho d}bN_n(k_{\rho d}b)}$$

$$\Delta_4=\frac{J_n(k_{\rho d}b)}{N_n(k_{\rho d}b)} \qquad \Delta_9=-\frac{I_n'(k_\rho a)}{k_\rho aI_n(k_\rho a)}$$

$$T=(1/k_{\rho d}b)^2+(1/k_{\rho d}b)^2$$

$$Q=\frac{k_{\rho d}^2+k_\rho^2}{k_{\rho d}^2+\varepsilon_rk_\rho^2}$$

Numerical Solution

Equation (4.14) is solved using the same method as the one described in Section 4.2 for dielectric rods. The results for the relative phase velocity, v/c, versus the normalized circumference of the tube, $2\pi b/\lambda$, for the HE_{11} mode for tubes having the dielectric constant $\varepsilon_r = 11.2$ and inner to outer radii ratios $a/b = 0.32, 0.5$, and 0.7 are plotted in Fig. 4.4. Similar to the dielectric rods, the phase velocity of tubes with small outer radius is close to the speed of light in free space. However, it decreases with increasing outer radius. The rate of this reduction is greater for tubes with thicker wall. Furthermore, for a tube of given external diameter and dielectric constant, the axial phase velocity increases when the wall thickness decreases (a/b increases). Hence, the phase velocity in a solid rod with $a/b = 0$,

is less than the phase velocity in a tube with the same dielectric constant and outer radius as the dielectric rod. These are expected phenomena since the phase velocity is dependent on the effective permittivity of the waveguide medium. The less effective permittivity of the waveguide medium would support the traveling waves with higher phase velocity. The effective permittivity for unit volume of a dielectric tube decreases as the a/b ratio increases. Hence, the phase velocity is higher for dielectric tubes with higher a/b ratio. This is also clear by comparing Fig. 4.1 and 4.4.

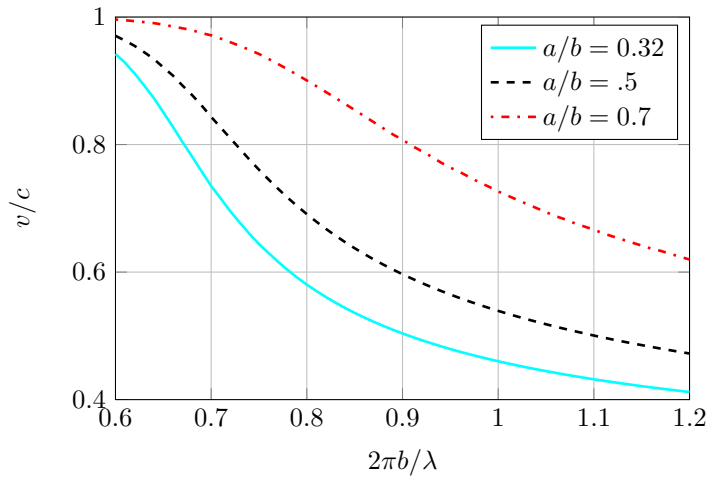

Figure 4.4: Normalized phase velocity of the HE_{11} surface eave mode in dielectric tubes of dielectric constant $\varepsilon_r = 11.2$ and for three different inner to outer radii ratios, $a/b = 0.32, 0.5$ and 0.7, as a function of the normalized circumference of the tubes.

Chapter 5

Polarization of Antennas

5.1 Introduction

The polarization of an antenna in a given direction is defined as the polarization of the fields radiated by the antenna in that direction [58]. Practically, the polarization of the radiated wave varies with the direction of radiation with respect to the antenna. Therefore, different points of the antenna radiation pattern may have different polarizations. In the case that the direction is not mentioned, the polarization is taken to be the polarization in the direction of maximum radiation intensity [58].

The polarization of an antenna is a far-field quantity where the radiated waves by the antenna are usually approximated by plane waves. Hence, the polarization of an antenna is the same as the polarization of the plane wave that approximates the radiated wave by the antenna in the far-field region.

The polarization of a time harmonic uniform plane wave describes the time varying behavior of the electric field intensity vector over one period of oscillation at a given point in space [60]. The polarization of an electromagnetic field is important in many practical applications, such as [61]

- For the purpose of optimizing the propagation through a selective medium (such as the ionosphere) or optimizing the back scattering off a target. This places a constraint on the design of a transmitting antenna.

- The polarization of an incoming wave may have to be accepted (which places a constraint on the design of the receiving antenna that will receive this wave optimally).

- The polarization of an incoming wave may be unpredictable (it is desirable in this case to design a receiving antenna which will respond equally to all polarizations).

In order to deal with problems similar to that mentioned above, it is necessary to define, describe, and quantify the polarization of an electromagnetic wave.

5.2 Linear, Circular, and Elliptical Polarizations

There are in general two types of antennas: Type **I** antennas of which the actual current distribution is well known like dipoles and helices. Type **II** antennas are those for which the actual current distribution is difficult to deduce, but they could be enclosed by a surface over which the fields are known with reasonable accuracy, such as horns and slots. In either case, the far field pattern of a transmitting antenna can be viewed as the product of an outgoing spherical wave in a complex directional weighting function [61]. The electric field at a far-field distance can be represented by

$$\mathbf{E} = (\hat{\mathbf{a}}_\theta E_\theta + \hat{\mathbf{a}}_\phi E_\phi)\, e^{\mathrm{j}\omega t}, \tag{5.1}$$

for time harmonic sources.

The functions $E_\theta(r,\theta,\phi)$ and $E_\phi(r,\theta,\phi)$ are in general complex:

$$E_\theta = E'_\theta + \mathrm{j}E''_\theta \tag{5.2}$$

$$E_\phi = E'_\phi + \mathrm{j}E''_\phi. \tag{5.3}$$

The instantaneous field can then be written as

$$\mathscr{E}(r,\theta,\phi,t) = \Re[\mathbf{E}] = \hat{\mathbf{a}}_\theta(E'_\theta \cos\omega t - E''_\theta \sin\omega t) + \hat{\mathbf{a}}_\phi(E'_\phi \cos\omega t - E''_\phi \sin\omega t), \tag{5.4}$$

where E'_θ, E''_θ, E'_ϕ, and E''_ϕ are real valued functions of the spherical coordinates, r, θ, and ϕ.

Equation (5.4) can be written in the form

$$\mathscr{E}(r,\theta,\phi,t) = \hat{\mathbf{a}}_\theta A\cos(\omega t+\alpha) + \hat{\mathbf{a}}_\phi B\cos(\omega t+\beta), \tag{5.5}$$

in which

$$A = \sqrt{(E'_\theta)^2 + (E''_\theta)^2} \qquad B = \sqrt{(E'_\phi)^2 + (E''_\phi)^2}$$

$$\alpha = \arctan\frac{E''_\theta}{E'_\theta} \qquad \beta = \arctan\frac{E''_\phi}{E'_\phi}. \tag{5.6}$$

With no loss in generality, the origin of time can be chosen such that $\alpha = 0$. Hence, (5.5) can be written as

$$\mathscr{E}(r,\theta,\phi,t) = \hat{\mathbf{a}}_\theta A\cos\omega t + \hat{\mathbf{a}}_\phi B\cos(\omega t+\beta). \tag{5.7}$$

In general, the polarization of an electromagnetic wave is elliptical. This means the curve traced by the end point of the electric field vector arrow, at a given position, as a function of time, is an ellipse. Two important specific cases of elliptical polarization are linear polarization and circular polarization. An electromagnetic wave is said to be linearly polarized when

$$\beta = n\pi, \qquad n = 1, 2, 3, \ldots \tag{5.8}$$

Linear polarization is that specific type of elliptical polarization when the minor axis of the ellipse is zero. Anther specific situation occurs when

$$A = B, \qquad \& \qquad \beta = \pm(n + \frac{1}{2})\pi, \tag{5.9}$$

which is known as circular polarization condition. This is also a particular case of elliptical polarization: when the major and minor axis of the ellipse are equal.

5.3 The Axial Ratio

It was mentioned in Section 5.2 that the most general case for the polarization of a plane wave is elliptical polarization. In this case, the curve traced by the end point of the electric field vector at a given position as a function of time is a tilted ellipse. The ratio of the major axis to the minor axis of the polarization ellipse is referred to as the axial ratio (AR).

Based on (5.7), the magnitude of the instantaneous electric field is given by:

$$|\mathscr{E}(r, \theta, \phi, t)| = \left[A^2 \cos^2 \omega t + B^2 \cos^2(\omega t + \beta)\right]^{1/2}. \tag{5.10}$$

If the time derivative of this function is set equal to zero, the maximum and minimum of $|\mathscr{E}(r, \theta, \phi, t)|$ can be identified. They occur at angles $\omega t = \tau$ governed by

$$\tan 2\tau = -\frac{B^2 \sin 2\beta}{A^2 + B^2 \cos 2\beta}. \tag{5.11}$$

If the first and second solutions of (5.11) are τ_1 and τ_2, then $|\tau_1 - \tau_2| = \pi/2$. This means that the direction of maximum and minimum magnitude of the electric field are at right angles to each other. This is to be expected since they are indeed the principal axes of the ellipse traced by the electric field vector. The magnitudes of semi-major and semi-minor axes can be found by substituting τ_1 and τ_2 into (5.10). This gives [61]

$$|\mathscr{E}| = \left[\frac{A^2 + B^2}{2} \pm \left(\frac{B^2}{2}\right) \frac{\sin 2\beta}{\sin 2\tau_1}\right]^{1/2}. \tag{5.12}$$

Equation (5.7) indicates that, excluding linear polarization as an exceptional case, $|\mathscr{E}(r,\theta,\phi,t)|$ rotates at a uniform rate with an angular velocity ω in the $\theta-\phi$ plane. If the fingers of the right hand follow the direction of the rotation and the thumb points to the direction of propagation, the wave is right hand elliptically polarized. Otherwise, if the direction of rotation of $|\mathscr{E}|$ and propagation of the wave followed by the fingers and thumb of the left hand, the wave is left hand elliptically polarized. The same categorization exists for circularly polarized waves.

The axial-ratio of a plane wave can be determined using (5.12). This quantity is often measured in dB as

$$AR = 20\log\left(\frac{|\mathscr{E}|_{\max}}{|\mathscr{E}|_{\min}}\right) \tag{5.13}$$

The AR equals 0 dB for a circularly polarized wave and is infinite for a linearly polarized wave. However, an axial ratio less than or equal to 3 dB is usually considered as accruable value when a circularly polarized wave is required [37].

Circularly polarized antennas are preferred in various communication systems. This is due to the advantages provided by them as compared to linearly polarized antennas, such as greater flexibility in the orientation between the transmitter and receiver antennas and less sensitivity to propagation effects [62].

A circularly polarized wave can be synthesized from two spatially orthogonal linearly polarized waves that are in phase quadrature ($\pm\pi/2$ phase offset). An antenna capable of generating two linearly polarized wave that are spatially orthogonal and in phase quadrature will therefore generate a circularly polarized radiation.

Chapter 6

Results

In the first part of this thesis, a novel excitation technique for cylindrical dielectric resonator antennas is introduced to produce circular polarization. The exciter is a tape helix that is wound around the dielectric resonator and is fed by a coaxial probe. The geometry of the proposed antenna is illustrated in Fig. 6.1. The proposed architecture is a combination of two basic antenna structures, a helical antenna and a dielectric resonator antenna. Therefore, this new class of antenna offers characteristics that are shared between helical antennas and DRAs. The proposed antenna is more than regular unloaded helix antenna. The antenna bandwidth is wider than basic cylindrical DRAs and is also circularly polarized. This characteristic drives from the wide band circularly polarized nature of the helix to the DRA.

The operation of this class of antenna can be viewed in a more systematic way. As explained in Section 2.3, an external helix wound around a cylindrical DRA can be an efficient tool to excite the $HE_{11\delta}$ mode in a DRA. Furthermore, the helix is capable of exciting both of these modes that are in phase quadrature, due to its azimuthal symmetry. This leads to a circularly polarized radiation. As compared with other single feed cylindrical DRAs, the proposed antenna provides a broader 3 dB axial-ratio bandwidth.

The helix is naturally a wide band radiating structure. The band width of the proposed type of antenna is mainly restricted by the DRA rather than the helix. Hence, in order to enhance the antenna bandwidth, the bandwidth of the DRA should be enhanced. Some of the methods used to enhance the bandwidth of the cylindrical DRAs can also be employed to develop the proposed class of antenna. Among these techniques, removing the central portion of the dielectric cylinder to create a dielectric ring and also utilizing stacked cylindrical DRAs are investigated in this thesis. They both are shown to perform well in the impedance and 3 dB axial-ratio bandwidths enhancement of the proposed type of antenna.

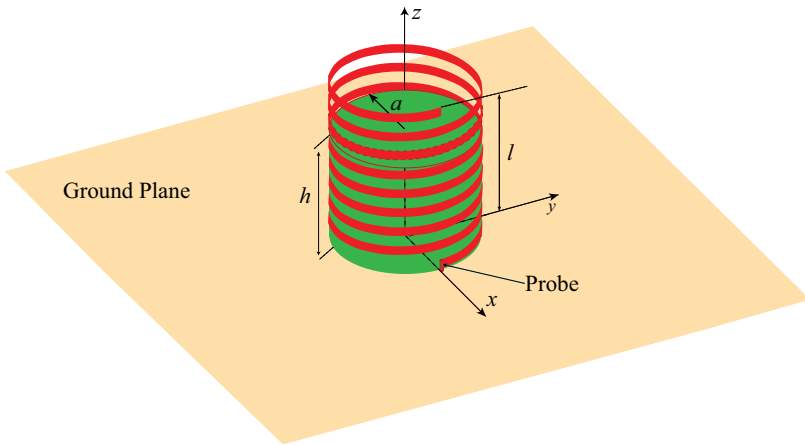

Figure 6.1: The configuration of a cylindrical DRA excited by a helix.

6.1 Design

In the proposed class of antenna, the helix excites the $HE_{11\delta}$ modes in the cylindrical DRA. The resonance frequency of the antenna structure can be estimated from the general formula for $HE_{11\delta}$ modes in a cylindrical DRA [62],

$$\frac{2\pi a}{\lambda_r} = 2.735\varepsilon_r^{-0.436}[0.543 + 0.589x - 0.050x^2], \tag{6.1}$$

where $x = a/2h$ and λ_r is the wavelength at the resonant frequency in free space.

The proposed antenna is a hybrid antenna that consists of two classic radiating architectures: a helical antenna and a DRA. In order for the antenna to function properly, the two elements are required to have similar radiation characteristics. A typical radiation pattern of the $HE_{11\delta}$ modes in a cylindrical DRA is shown in Fig. 6.2(a). Typical radiation patterns for normal mode and axial mode helix antenna are also illustrated in Fig. 6.2 (b) and (c) respectively. It can be observed that the radiation pattern of the $HE_{11\delta}$ modes DRA and axial mode helix are broad-side, while for the normal mode helix the pattern is omnidirectional. Hence, in order for the antenna to function properly, the helix is required to operate in its axial mode to be compatible with the radiation characteristics of the $HE_{11\delta}$ modes. As mentioned in Chapter 3, the radiation pattern for the axial mode helix antenna can be well approximated with the Hansen–Woodyard increased directivity condition for linear phase arrays. The Hansen–Woodyard condition (3.5) for the helix in Fig. 6.1, considering the image theorem with respect to the conducting ground plane can be written as

$$\frac{2l}{\pi a}\left[\frac{c}{v}-1\right]=\frac{\lambda}{2\pi a}, \tag{6.2}$$

where λ is the wavelength in free space, c is the free space phase velocity, and v is the surface wave phase velocity along the z axis.

The phase velocity, v, is the $HE_{11\delta}$ mode surface wave phase velocity along the side wall of the DRA. This phase velocity can be estimated from the axial phase constant of the HE_{11} surface wave mode in an infinite dielectric rod with the same permittivity and radius as the dielectric resonator. The solution for the phase constant in a dielectric rod was discussed in Section 4.2.

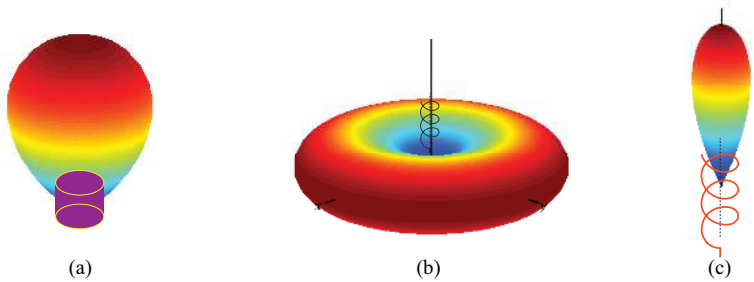

Figure 6.2: Typical schematic radiation pattern of (a) the HE_{11} modes in a cylindrical DRA, (b) normal mode helix and (c) axial mode helix.

The proposed antenna has five major design parameters: the radius a, the height h, the permittivity of the cylindrical dielectric resonator ε_r, the pitch s, and the number of turns of the helix exciter, N. Based on the above mentioned information from the proposed class of antenna, design guidelines are provided. The guidelines give a starting point for the design. Given the dielectric constant of the cylindrical dielectric resonator, the design process can be formulated as follows.

- The ratio h/a is uniquely determined in terms of $2\pi a/\lambda$ from (6.1).
- Plot the phase velocity of the HE_{11} mode in a cylindrical dielectric rod with the given permittivity as a function of the normalized circumference of the rod. The ratio l/a is uniquely determined in terms of $2\pi a/\lambda$ from the intersection of the HE_{11} mode phase velocity curve and the Hansen–Woodyard phase velocity (6.2).

- Choose a value for $2\pi a/\lambda$ close to the upper bound of the helix axial mode(see Fig. 6.4). [1]
- Find the corresponding value for l/a at the chosen $2\pi a/\lambda$.
- From the chosen l/a, go down towards the $2\pi a/\lambda$ axis by the amount ΔC [2] . At this new point find the corresponding value for h/a.

The total height of the helix depends on the probe height, the pitch angle and the number of turns. Our investigations indicate that the probe height should be as short as possible. The best values for the number of turns in the helix are within the interval $5.5 \leq N \leq 8.5$. However, the most repeated optimized value for the number of turn is $N = 8$. The pitch angles can then be adjusted when the total height and the number of turns are known.

The design guideline is provided for the normalized DRA radius a/λ. For a desired operation frequency, the physical dimension of the radius can be determined.

This guidelines is followed here to find a starting point for the deign of three antennas of the proposed type with three different dielectric constants. The starting points are then optimized for the widest 3 dB axial-ratio bandwidth using HFSS. The normalized phase velocities of the HE_{11} surface wave mode on infinite rod of permittivities $\varepsilon_r = 5, 10$ and 20 are plotted in Fig. 6.3, as functions of the normalized circumference of the rods. The normalized phase velocities for the Hansen–Woodyard condition with the optimized value of a/l for each case are also plotted. It can be observed that for lower dielectric constants a larger DRA radius and taller helix height are needed for the Hansen–Woodyard condition to intersect with the HE_{11} mode curve in the proper region. The values for h/a and l/a determined from (6.1) and matching phase velocities of HE_{11} and the Hansen–Woodyard condition respectively, are plotted as a function of $2\pi/a$ for $\varepsilon_r = 10$. The red and black circles show the optimized values for l/a and h/a respectively. The distance $\Delta C = 0.9(2\pi a/\lambda_w)$ for the optimized points. The coefficient 0.9 agrees well with the rule of thumb mentioned in the guidelines, corresponding to one-half of the impedance bandwidth. The values are scaled to operate at $f \sim 2.8$ GHz. The optimized parameter values of the three designs and the resulting 3 dB axial-ratio and impedance bandwidth for each case are summarized in Table 6.1. As listed in

[1] It should be noted that this upper bound for an unloaded helical antenna is roughly $2\pi a/\lambda \sim 1.3$. However, our case studies indicate that this value shifts downwards if the helix is loaded with a dielectric core. The amount of this shift is proportional to the guided wavelength in the dielectric supporter of the helix. When putting a dielectric resonator with permittivity $\varepsilon_r \sim 10$ at the launching point of the helix, this upper bound reduces to $2\pi a/\lambda \sim 0.9$. The upper bound for $\varepsilon_r \sim 20$ is $2\pi a/\lambda \sim 0.6$.

[2] The percentage ΔC is supposed to be equal to one-half of the antenna band width. The proposed antenna bandwidth for a cylindrical DRA with dielectric constant $\varepsilon_r \sim 10$ is on the order of 16%. The quality factor of the $HE_{11\delta}$ in a cylindrical DRA varies with the dielectric constant of the DRA as $\varepsilon_r^{1.202}$. The bandwidth variation with the the dielectric constant of the DRA can then be well estimated as $\varepsilon_r^{-1.202}$

the table, the antenna with lower dielectric constant provides a wider impedance and 3 dB axial-ratio bandwidth.

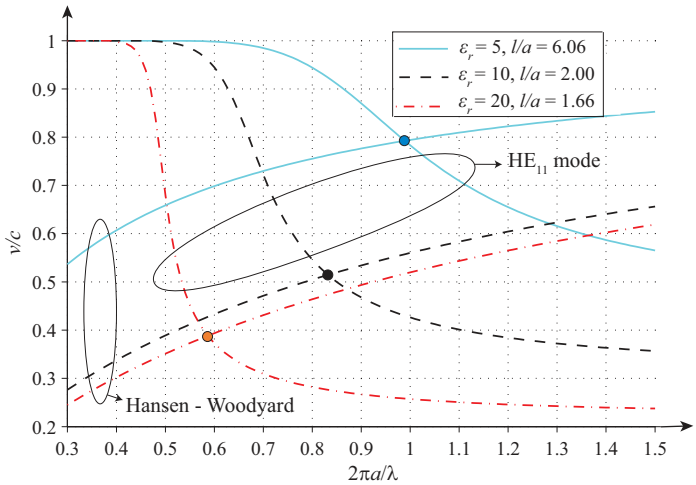

Figure 6.3: The normalized phase velocity of the HE_{11} modes on infinite dielectric rod of three different values for dielectric constant together with the normalized phase velocities of the Hansen–Woodyard condition for DRA designs with the same permittivity as used for the rods.

	Case # 1	Case # 2	Case # 3
ε_r (mm)	5	10	20
a (mm)	16	13	10
h (mm)	60	18	12.2
l (mm)	9.7	25.8	16.6
N	8	8	7.8
s (mm)	12	3.1	2.0
f_r (GHz)	2.7	2.8	2.8
f_w (GHz)	2.98	3.0	2.9
$f_l - f_h$ (GHz)	2.1–3.3	2.6–3.04	2.89–3.05
Impedance BW	44 %	15.6 %	4.4 %
Axial Ratio BW	28 %	6.4 %	2.9 %

Table 6.1: Design parameters and corresponding simulation results three design cases for 3 antennas of the proposed type with cylindrical DRA.

Similar design guidelines as discussed for the cylindrical DRAs can be followed to design the proposed type of antenna using a ring DRA. However, in the case of ring DRA, in addition to the dielectric constant, the inner to outer radius ratio is also

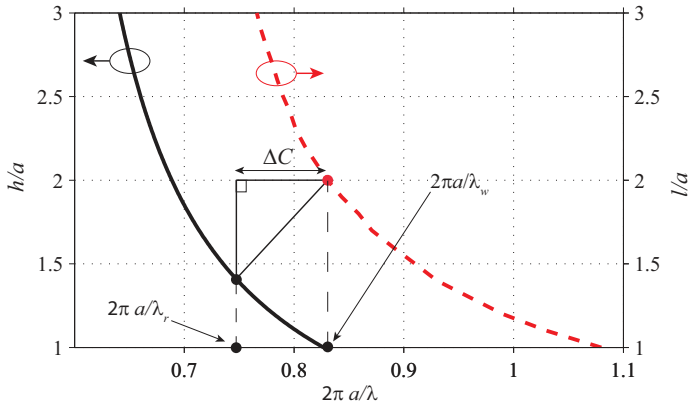

Figure 6.4: The schematic illustration of the design guidelines for the case #1. The non-right apexes of the triangle in the figure show the optimized values for l/a and h/a.

required to start the design process. For the ring DRA, the dielectric constant ε_r in the resonance frequency formula (6.1) must be replaced by the effective permittivity of ring DRA, which can be estimated by

$$\varepsilon_{r\text{eff}} = \frac{\left(a^2 - b^2\right)\varepsilon_r + b^2}{a^2}, \tag{6.3}$$

where ε_r, a, and b are the dielectric constant, the outer radius of the ring and the inner radius of the ring, respectively.

The phase velocity, v, in (6.2) for the ring DRA case can be estimated from the axial phase constant of the HE_{11} surface wave mode in an infinite dielectric tube with similar permittivity, inner and outer radii as the corresponding ring dielectric resonator. The solution process for the phase constant of a dielectric tube was explained in Section 4.3 and the numerical results were also plotted in Fig. 4.4. These plots refer to tubes of permittivity ε_r and inner to outer radius ratios of $a/b = 3.2, 0.7$ and 0.5. Three antennas of the proposed type are designed using dielectric rings of the dielectric constant and inner to outer ratio as of the tubes reported in Fig. 4.4. The outer radii for all cases are the same and equal to $b = 8.25$ mm. The curves of Fig. 4.4 are again shown here in Fig. 6.5, this time together with the normalized phase velocities for the Hansen–Woodyard condition with the optimize value of l/a for each of the designed antenna case. It can be observed that for greater a/b, a taller helix height is required for the Hansen–Woodyard condition to intersect with the HE_{11} mode curve in the proper region. The optimized parameter values of the three designs and the resulting 3 dB axial-ratio and impedance bandwidth for each case are summarized in Table 6.1. As

listed in the table, the antenna with greater a/b ratio provides a wider impedance and 3 dB axial-ratio bandwidth.

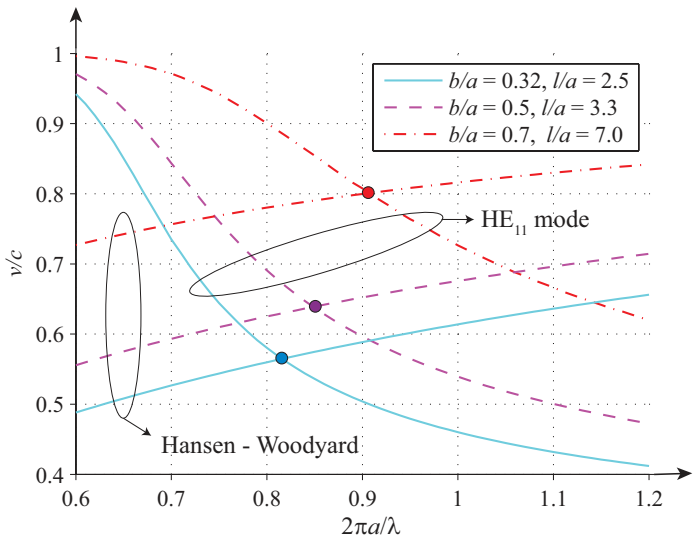

Figure 6.5: The normalized phase velocity of the HE_{11} modes on infinite dielectric tubes of three different b/a ratio with dielectric constant of $\varepsilon_r = 11.2$ together with the phase velocities of to the corresponding Hansen–Woodyard condition.

	Case # 1	Case # 2	Case # 3
b (mm)	5.8	4.12	2.65
h (mm)	40	12	14
l (mm)	57.5	27.0	20.6
N	8.25	8	8
s (mm)	6.8	3.2	2.5
f_r (GHz)	4.32	4.57	4.1
f_w (GHz)	5.26	4.92	4.75
$f_l - f_h$ (GHz)	3.8–6.0	4.46–5.64	4.21–4.89
Impedance BW	45 %	23 %	15 %
Axial Ratio BW	24 %	15.8 %	7.2 %

Table 6.2: Design parameters and corresponding simulation results three design cases for 3 antennas of the proposed type. For all of the designs $a = 8.25$ mm and $\varepsilon_r = 11.2$.

6.2 Fabrication and Measurement

For both the cylindrical and ring (hollow cylindrical) cases, prototypes were fabricated and measured. The dielectric resonators were purchased from T-ceram company. The height of the DRA and helix exciter are specified by different phenomena. The height of the DRA, h, is obtained from its resonance condition while for the helix exciter, the total height, l, is given by the Hansen–Woodyard condition. Since the radius of the DRA is restricted to be in the helix axial mode interval, this usually ends being to a greater height for the helix rather than the DRA. In order to support the tape helix on the top of the DRA, a Rohacell foam material from Evonik was used. The dielectric constant of the Rohacell foam is 1.04, which is very close to the free space permittivity. The cylindrical shape supporters with the required sizes were cut out from a Rohacell fiber using scraped metallic pipes of the proper diameter as shown in Fig. 6.6(a). Fig. 6.6(b) shows some of the dielectric resonator as well as cylindrical cuts of Rohacell foam. The helical exciters in the fabricated prototypes are made out of a copper tape. A narrow strip was clipped out from a copper tape using a double blade razor as shown in Fig. 6.6(c). Superglue was used to attach the Rohacell foam on top of the ceramic dielectric resonator and also to stick the ceramic dielectric resonator on the copper ground plane. One of the fabricated prototypes is shown in Fig. 6.7(a).

The return loss of the fabricated antennas was measured by an Anritsu MS2026B series network analyzer. For measurement of the far-field parameters a horn transmitter antenna was used. A robot positioner was employed to sweep over the azimuth, ϕ, and elevation, θ, angles. The antenna was mounted on the robot as shown Fig. 6.7(b). For the radiation pattern measurement the antenna was rotated around x or y axis with $\theta = 2^\circ$ precision. The measured data were recorded on the network analyzer and then synthesized by a MATLAB program to produce the radiation pattern of the antenna.

The axial ratio measurement is more complicated. As explained in Section 5.3, the axial ratio (AR) is defined as the ratio of the major axis to the minor axis of the elliptical curve traced by the end point of the electric field vector. To detect the ellipse that is traced by the electric field, the antenna was rotated on the robot around the z axis and measured and recorded the fields at each point. The recorded points should ideally be located on an ellipse. However, because of noise and imperfect experimental instruments they have offset. In order to detect the most likely elliptical curve representing the electric field rotation a root mean square optimization process was employed. The ratio of the major and minor axes of the detected ellipse gives an estimate for the measured AR of the antenna. For the cylindrical DRA case the simulation and measured results for the return loss and the axial ratio are shown in Fig. 6.8 and 6.9, respectively. It can be observed that the measured and simulation results are in good agreement. The detailed results for both of the fabricated antennas can be found in Papers I and II.

(a)

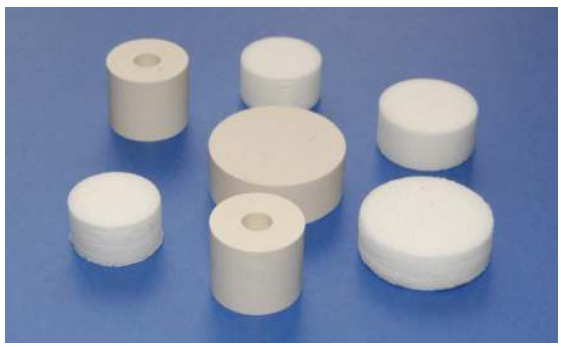

(b)

(c)

Figure 6.6: (a) Rohacell fibre and the pipe used for cutting cylindrical pieces, (b) Cylindrical ceramic resonators and foam cuts, (c) Double blade employed to clip a narrow strip out of a copper tape.

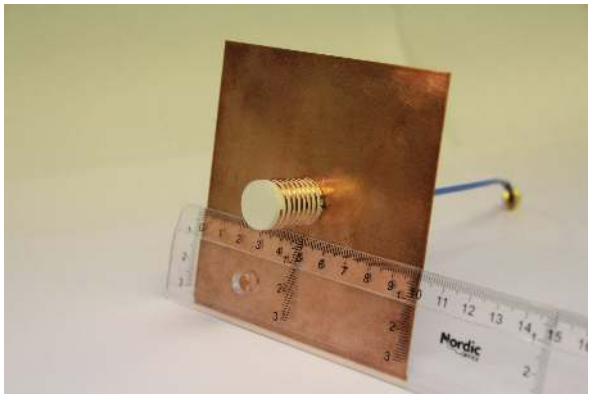

(a)

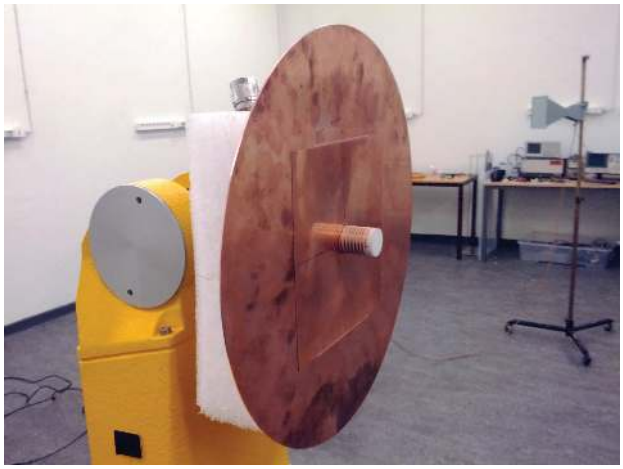

(b)

Figure 6.7: (a) Fabricated antenna and (b) The fabricated antenna on a robot for the axial ratio and radiation pattern measurement

6.3 Contribution

In this thesis a new class of hybrid antenna, consisting of a helix and a dielectric resonator antenna, was introduced. Although the helix loaded dielectric core is not a new subject, there are, as far as the author knows, no systematic investigation on the design process, limitations and advantages together with a modal study on the dielectric core in the literature on this type of antenna.

Previously, similar problems on helix loaded dielectric have been investigated.

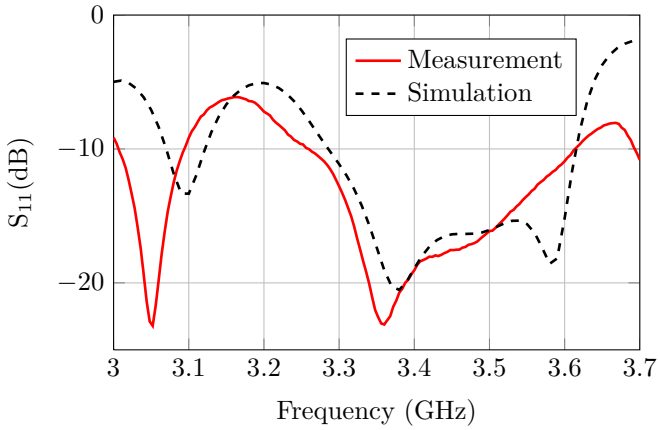

Figure 6.8: Simulation and measurement results for reflection coefficient of the helix fed cylindrical DRA

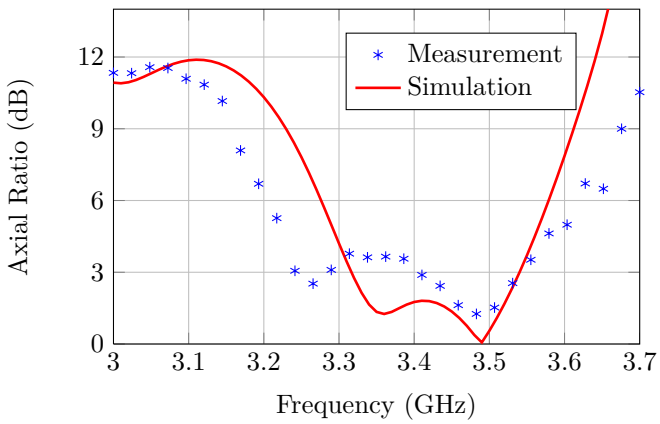

Figure 6.9: Simulation and measurement results for the axial-ratio of the helix fed cylindrical DRA

In [63], a moment method is used to analyze a helical antenna loaded by a dielectric resonator. In that paper, the helix does not touch the dielectric resonator core and the effects due to the existence of a dielectric core and its distance from the ground plane on a helical antenna parameters is studied. However, the authors did not provide any optimal design for a dielectric loaded helix. That paper mostly concentrates on the solution method rather than the design performance.

A reduced size helical antenna is presented in [64]. In this work, a bi-filar helix

is introduced that is operating in the backfire mode. Two matching strips are used to improve the impedance bandwidth. Although a dielectric supporter is used to reduce the helix size, there is no relation provided between the reduced size and the characteristic of the dielectric supporter.

The radiation characteristics of an axial mode helix loaded with a dielectric core is considered in [65]. A network model is used to model the antenna as a surface wave structure. A dielectric core is included to decrease the cross polarized radiation in the off-axis directions.

In all of the above-mentioned papers, the resonance condition of the dielectric resonator cores are not included in the design, probably due to their wide-band nature related to their low permittivity. Furthermore, none of them provides a relation between the supporting dielectric core and the height of the helix. In [63], the authors introduce the helix as a useful exciting element for a dielectric rod antenna and comment on the excited modes in the dielectric rod. However, the height of the rod in that paper is much longer than the helix and the dielectric constant is also low. Also, in this case, the resonance condition of the dielectric rod is ignored, possibly due to the wide-band nature of the low dielectric constant supporter. Moreover, there is no ground plane included in this traveling wave antenna structure.

In this thesis, we provide an approach to estimate the height of the helix as a function of the dielectric core characteristics located at the launching point of the helix. The approach is based on the phase velocity of the surface wave traveling along the side wall of the dielectric resonator core. This phase velocity is estimated from the solution of a dielectric rod with the permittivity and radius as the dielectric resonator core. From a dielectric resonator antenna point of view, the proposed antenna is a single point feed cylindrical DRA that provides a larger 3 dB axial ratio bandwidth as compared to the other reported single point feed antennas [37,66,67]. Several antennas of this type are designed and some of them are reported in Paper I. The proposed helical type of excitation can also be used to excite circularly polarized surface waves on other types of dielectric resonator antennas, such as for a ring (hollow cylindrical) DRA. A ring DRA supports surface waves with higher phase velocity than a similar cylindrical DRA. This leads to a size enlargement in the DRA but at the same time an increase in the impedance and the 3 dB axial-ratio bandwidth of the antenna. This phenomenon is discussed in Paper II.

6.4 Conclusion

In the first part of this thesis a novel excitation method was introduced for cylindrical dielectric resonator antennas. The proposed type of antenna produces a circularly polarized radiation. The exciter of the antenna is a tape helix that is wound around the dielectric resonator and is fed by a coaxial probe. As compared to other single feed DRAs, the proposed method offers a wider impedance and 3 dB axial-ratio bandwidths. The circularly polarized wave produced by the antenna is

the outcome of the excitation of two orthogonal $HE_{11\delta}$ surface wave modes in phase quadrature in the cylindrical DRA. Design guidelines were provided and employed to create several design cases of the proposed type of antenna. The design guidelines are based on the phase velocity of the single traveling surface along the side wall of the DRA together with the Hansen–Woodyard increased directivity condition together with the general formula for the resonance frequency of the $HE_{11\delta}$ mode in cylindrical DRAs. Initial values of the design parameters were estimated using the presented design guidelines. The optimal values for the parameters were then found using HFSS. One of the simulated design examples has been fabricated and agreed well with the simulation results. The helix was also used to excite $HE_{11\delta}$ modes in ring DRAs. As compared with a cylindrical DRA, using the ring leads to a wider impedance and 3 dB axial-ratio bandwidth and at the same time the antenna requires a taller helix exciter to function properly.

The proposed antenna is compact, uncomplicated, low cost, and easy to fabricate. The invention of this antenna can be the basis of several interesting research problems. Many ideas for improving cylindrical DRAs can also be used in this type of hybrid antenna. We used two methods for bandwidth enhancement: stacking and removing the central portion of the cylindrical DRA, in this thesis. Terminating the helix with a spiral strip on the top of the cylindrical DRA, using a bi-filar helix, more investigation on the effects of the pitch angle, using conical shape DRAs, the effects of tapering of the helix, and many interesting ideas in antenna design can be applied to this type of antenna as a single element. The proposed type of antenna can also be used and investigated as an array element.

Part II

General Introduction to A Polarization Sensitive Rasorber Design

Chapter 7

Statement of the Problem

7.1 Background

Reducing radar visibility is a factor in the survivability of military targets. As a consequence, stealth or invisibility to radar is of widespread interest to researchers [68, 69]. A common method to reduce the radar signature of a target is to protect the target with radar absorbing materials. As is implied from the name, radar absorbing materials reduce the reflected power back to the radar receiver antenna by means of absorption of the electromagnetic energy.

For some applications, such as protecting an antenna from detection by the radar waves by a radome, the radar absorber is required to absorb electromagnetic waves at the radar detecting waves while being transparent for the frequencies at which the protected antenna operates. Such structures are called absorbers with windows. They are also known as Rasorbers [70] that is a combination of words radome and absorber.

It is common to divide absorbers into two classes: magnetic absorbers and electric absorbers. In both cases a lossy electric or magnetic sheet is placed at the location of the maximum electric or magnetic field respectively. In the case of reducing the reflection from a perfect electric conductor (PEC) surface the maximum electric field occurs at a quarter of a wavelength away from the PEC surface while the magnetic field has its maximum on the PEC surface. Therefore, for an electric absorber, a screen having a matched resistivity is positioned a quarter of a wavelength apart in front of the metallic plate. These designs are often referred to as Salisbury screens [71]. A magnetic lossy sheet can be placed directly onto the PEC surface. A consequence of the absorber lossy sheet position is that a Salisbury absorber is thicker than a magnetic absorber. Furthermore, the Salisbury absorbers are efficient only for a narrow frequency band because of their resonant nature. However, the magnetic absorbers are often heavy and fragile [72], making them inappropriate for flying structures. Furthermore, it is difficult to find materials that meet particular desired conditions and they often have a strong frequency

variation [73]. Another complication is that the magnetic lossy sheet must have enough low intrinsic impedance to let the incident radiation penetrate so that the conductor will be effective at establishing a boundary condition that positions the maximum magnetic field within the lossy sheet.

There are ongoing research efforts to overcome problems with magnetic absorbers, see, e.g., [72, 74, 75]. The bandwidth of a Salisbury screen can be improved by adding extra resistive sheets and dielectric spacers to form a Jaumann absorber [71, 73]. The reason for this improvement is to create an extra resonance in the screen structure which increases the bandwidth of efficient absorption.

The main blocking part of Salisbury and Jaumann absorbers is the PEC backing surface. Hence, the first step to introduce a transparent window in a conventional absorber is to replace the PEC surface with a structure that is as transparent as possible for the waves of the transparent window frequency while providing a PEC-like behavior for the other frequencies, to enable the absorption phenomenon.

7.2 Design Goals

The subject of this part of the thesis is to design a rasorber with different requirements for two orthogonal linear polarizations. The rasorber is required to have a transparent window at 1 GHz for one of the polarizations and provide as much absorption as possible for the other frequencies in the band of interest with this polarization and also for all frequencies in this band with the other polarization. The frequency band of interest in this problem is 1–20 GHz.

Several constraints should be considered in the design process, such as the widest possible -20 dB absorption bandwidth, the highest transmission coefficient and the lowest loss at the transparent window, and also the smallest structure thickness.

In the next chapter, the theories and tools that have been used in the rsorber design process will be briefly presented.

Chapter 8

Analysis of Stratified Periodic Structures

In order to design the rasorbers presented in this thesis, two approaches were used in parallel: a wave splinting method and a full wave simulation using HFSS commercial software. The wave splitting method provides a fast approach to optimize the rasorber as a stratified structure. The full wave HFSS simulations were used to verify the results and also to synthesize the approximate model given by the wave splitting method. In this chapter, a brief description of these methods as applied to planar stratified structures will be presented.

8.1 Wave Splitting Method for the Analysis of Stratified Structures

The major part of the investigations in the second part of this thesis is on planar stratified structures. In the case of rasorber design, the parameters of the structure are optimized for the required reflection and transmission coefficients over a wide frequency band. The full-wave analysis of a planar structure for such a multidimensional optimization in a scattering problem for a wide frequency band can be computationally intensive and time consuming. For these problems it is more convenient to use an approximate method to reduce the computation time of the optimization problem.

In this chapter, a wave splitting technique [73, 76–78] will be introduced. This approach is based on assuming a certain form of the electric and magnetic fields on both sides of the impedance boundary in the dielectric layers of a stratified structure and on specifying the required boundary conditions that the fields must satisfy. This technique provides a fast method to obtain the transmission and reflection coefficients as functions of the boundary impedances and layer thickness of a normally illuminated stratified structure.

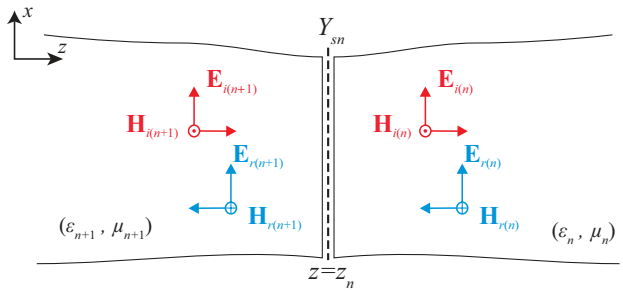

Figure 8.1: An impedance sheet sandwiched between two dielectric layers in a stratified media.

Consider a planar stratified structure of lossless, non-dispersive homogenous dielectric medium. Admittance sheets of an idealized zero thickness are sandwiched between the dielectric layers. The layers are parallel to the xy-plane and the structure is exposed to an incident plane wave traveling in z direction. Fig. 8.1 shows two adjacent layers of such a stratified structure. The electric and magnetic fields for an incident plane wave traveling in the positive $z-$direction in the n:th layer, assuming a time variation factor $\exp(\mathrm{j}\omega t)$, can be expressed as forward and backward propagating waves:

$$\mathbf{E}_n(z) = \hat{\mathbf{a}}_x[E_{i(n)}\exp(-jk_nz) + E_{r(n)}\exp(jk_nz)], \tag{8.1}$$
$$\mathbf{H}_n(z) = \hat{\mathbf{a}}_yY_n[E_{i(n)}\exp(-jk_nz) - E_{r(n)}\exp(jk_nz)], \tag{8.2}$$

where k_n is the wave number and $Y_n = \sqrt{\varepsilon_n/\mu_n}$ is the intrinsic admittance in the n:th medium.

The tangential electric fields are continuous across the sheet, whereas the tangential magnetic field jumps by an amount proportional to the induced surface currents. These boundary conditions, to be satisfied at the interface, can be written as

$$Y_{sn}\mathbf{E}_n(z_n) = Y_{sn}\mathbf{E}_{n+1}(z_n) = \mathbf{J}_s, \tag{8.3}$$

$$-\hat{\mathbf{a}}_z \times (\mathbf{H}_{n-1} - \mathbf{H}_n) = \mathbf{J}_s, \tag{8.4}$$

where Y_{sn} is the complex admittance of the uniform sheet sandwiched between the n:th and $(n+1)$:th medium and $\mathbf{J}_s$ is the surface current flow of this admittance.

Substituting (8.1) and (8.2), into (8.3) and (8.4) gives

$$E_{i(n+1)} = \frac{\exp(jk_{n+1}z_n)}{2Y_{n+1}}[(Y_{n+1} + Y_n + Y_{sn})E_{i(n)}\exp(-jk_n z_n) + (Y_{n+1} - Y_n + Y_{sn})E_{r(n)}\exp(jk_n z_n)], \tag{8.5}$$

$$E_{r(n+1)} = \frac{\exp(-jk_{n+1}z_n)}{2Y_{n+1}}[(Y_{n+1} - Y_n - Y_{sn})E_{i(n)}\exp(-jk_n z_n) + (Y_{n+1} + Y_n - Y_{sn})E_{r(n)}\exp(jk_n z_n)]; \tag{8.6}$$

hence, the fields in each layer can be determined from the fields in its earlier layer.

Apart from the change of the fields at the impedance boundaries, we use a propagator to account for the dielectric layers. This propagator is a phase transformation that relates the fields on two sides of each dielectric layer and can be expressed in matrix form as

$$\begin{bmatrix} E_{i(n)}(z_n) \\ E_{i(n)}(z_n) \end{bmatrix} = \exp[-jk_n(z_n - z_{n-1})] \begin{bmatrix} 1 & 0 \\ 0 & 1 \end{bmatrix} \begin{bmatrix} E_{i(n)}(z_{n-1}) \\ E_{i(n)}(z_{n-1}) \end{bmatrix}. \tag{8.7}$$

This method enables us to find the fields in each layer from the known incident fields. The reflection and transmission coefficients can be determined from the forward and backward waves.

This algorithm has been implemented as a Matlab code in order to calculate the reflected and transmitted fields of an arbitrary normally illuminated stratified structure. This method provides a fast and efficient method for field determination that converts the three-dimensional scattering problem to a one-dimensional scattering problem approximation where several equivalent fast solution methods are applicable. The advantage of this method as compared to the transmission line model is that one can simultaneously determine both the reflected and transmitted wave in each layer.

The above mentioned method can be used to analyze a periodic structure that consists of frequency selective surfaces (FSSs)[1] in their architecture provided that the higher order Floquet modes do not propagate without attenuation. This condition puts a constraint on using the proposed method to analyze the periodic structures. To meet this constraint for a rectangular grid lattice FSS, the inter-element spacing should be less than or equal to one-half of the wavelength [71, 79].

[1]Frequency selective surfaces (FSSs) are two-dimensional periodic structures that consist of metallic patch elements printed on a thin dielectric layer or aperture elements within a metallic screen.

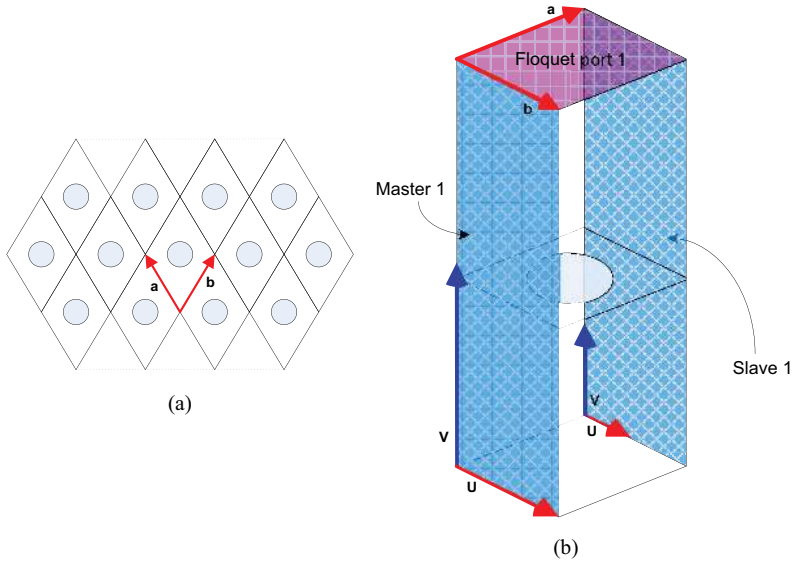

Figure 8.2: (a) Top view of a two dimensional periodic structure and (b) its simulated model schematic in HFSS, the Floquet port 2 at the bottom and the other Master / Slave boundaries are hidden for clarity of the picture.

8.2 Simulation of Periodic Structures in HFSS

The Floquet port in HFSS is exclusively used to analyze two-dimensional periodic structures. Using the Floquet port the analysis of an infinite periodic structures is achieved by analyzing a unit cell of the structure. In order to produce the periodic condition of the structure a Master/Slave boundary is used. The boundary condition of the master boundary is copied to its corresponding slave boundary. The angle of illumination of the periodic structure is assigned by setting the scan angle of the Master/Slave boundaries together with the lattice phase information of the Floquet ports. The vectors **a** and **b** which define the unit cell area are used to define a Floquet port on the top and bottom of the unit cell box as shown in Fig. 8.2. For clarity of the picture, only the top Floquet port and one Master/Slave boundary are shown in Fig. 8.2.

Chapter 9

Jaumann-Like Rasorber

A Jaumann absorber [71] is constructed by placing one or more resistive sheets spaced a quarter wavelength apart in front of a metal plane in a stratified medium. It has been shown that Jaumann absorbers effectively reduce the back scattering from planar [73] and curved structures [80] over a relatively wide frequency band. In this chapter the possibility of making a Jaumann absorber partially transparent at specific frequency and polarization is examined. This transparent window is basically achieved by replacing the main blocking part of the Jaumann absorber, the back PEC, with an appropriate frequency selective circuit.

9.1 Design

A Gangbuster-Polarizer FSS

In this section, an FSS with proper filtering behavior for incoming electromagnetic waves is designed. The desired structure should ideally be totally reflective for one linearly polarized wave while having a band-stop behavior for the polarization orthogonal to the first one. Furthermore, we are interested in a structure which is rather robust in functioning, so that its behavior persists when it is bent over curved surfaces. The band-stop behavior for one of the polarizations can be achieved by using a Gangbuster FSS [71] with dipoles parallel to the electric field of the incident wave. The Gangbuster structure can be superimposed with a periodic array of infinitely long strips as shown in Fig. 9.1(a). These infinite strips provide an almost perfect reflection for linearly polarized waves where the electric field is parallel to them. This cascading has no significant effect on the characteristics of the Gangbuster. In order to support the resulting structure, the Gangbuster dipoles and infinite strips of the polarizer are embedded into a dielectric slab. The cross section of the structure is shown in Fig. 9.1(b). Note that the Gangbuster dipoles and the polarized strips are not electrically connected to each other and are separated by a distance of $t/3$ inside the dielectric slab. The thickness and

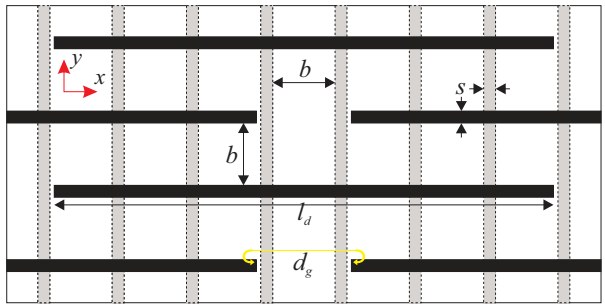

(a)

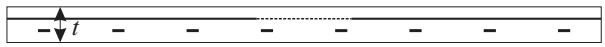

(b)

Figure 9.1: The cross-section of the FSS-backed Jaumann absorber.

periodicity of the infinite strips are chosen to be the same as for the Gangbuster dipoles.

The reflection from the above mentioned Gangbuster-FSS is illustrated in Fig. 9.2 for two orthogonal polarizations, $x-$ and $y-$ polarization. The $x-$ polarized waves are the linearly polarized incident plane waves with electric field in the direction of the $x-$ axis. The same standard is considered for the $y-$ polarized waves. The $x-$ and $y-$ coordinates are chosen as illustrated in Fig. 9.1(a). The values for the structure dimensions and the dielectric constant of the embedding dielectric slab are presented in the caption of this Fig. 9.2. As can be observed in the figure, we have obtained a high-reflection for the y-polarization over 1–16 GHz. For the x-polarization, we have obtained a transparent window at and below 1GHz with less than -10 dB reflection (the structure is lossless). The frequency response then rapidly reaches a high-reflection behavior over the frequency band between 3 and 15 GHz, with a reflection coefficient above -4 dB.

An Optimized Jaumann-Like Rasorber

A convenient backing FSS for the Jaumann-like rasorber has now been obtained. The next step of the design process is to integrate this FSS structure as a replacement of the metal-back layer of a Jaumann absorber. The structure is schematically illustrated in Fig. 9.3. The parameters of the structure, including the thickness and permittivity of the dielectric spacers as well as the resistive sheets should be determined such that the desired behavior is achieved. This desired behavior is the survival of the 1 GHz $x-$polarization transparency while keeping the absorption properties of the original Jaumann absorber for both the $x-$ and $y-$polarizations

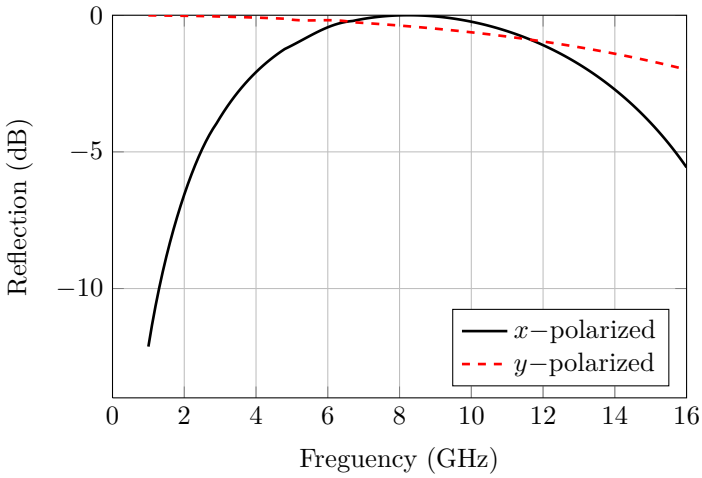

Figure 9.2: The full-wave simulation results for the reflection coefficient of the backing structure. $t = 1.5$ mm, $d_g = 3$ mm, $l_d = 8.4$ mm, $b = 3$ mm and $s = 0.4$ mm and $\varepsilon_{rs} = 2.2$

and for the frequency band 2–16 GHz. However, a high transmission coefficient at low frequencies for the $x-$polarization degrades the absorption at high frequencies and vice versa. Thus, the resulting structure will be a compromise between these two desired features. In order to reach such a compromise we have studied a series of cost-functions:

$$G(f) = \sum_{l=10}^{160} \max(\Gamma^{x-\mathrm{pol}}(f_0 + l\Delta f), -12) - w\mathrm{T}^{x-\mathrm{pol}}(f_0), \tag{9.1}$$

where $f_0 = 1$ GHz and $\Delta f = 0.1$ GHz, $\Gamma^{x-\mathrm{pol}}$ and $\mathrm{T}^{x-\mathrm{pol}}$ are the reflection and transmission coefficients, respectively, for the parallel polarization expressed in dB. The relative weight between the higher frequencies and the transmission coefficient at 1 GHz is controlled by the weight w to emphasize the importance of the required transmission at 1 GHz. Note that the cost function only contains the $x-$polarization. This choice of G requires fewer calculations resulting in a faster optimization process and the resulting design. The results show that the other polarization remain at least as good as the optimized one for frequencies above 3 GHz.

To accomplish this multidimensional optimization over a large frequency band is computationally intensive if a full wave analysis is implemented for each iteration. To avoid such a time consuming process, the structure is simulated and analyzed using the wave splitting method explained in Chapter 8. Since the dimensions of the FSS unit cell are smaller than a half wavelength over the entire operation

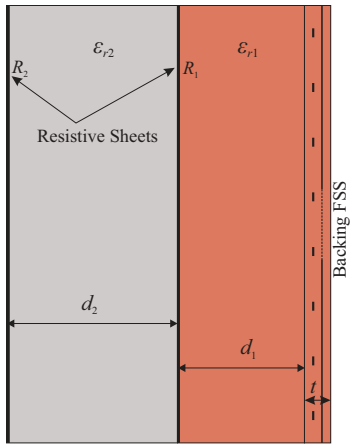

Figure 9.3: The cross-section of the FSS-backed Jaumann absorber.

bandwidth, the higher order Floquet modes cannot propagate without attenuation and the wave splitting method gives a good estimated solution for this stratified structure. The backing FSS in this model is replaced with an equivalent admittance obtained from HFSS numerical calculation of its reflection coefficient using [81]

$$Y_{\mathrm{FSS}}^{(x,y-\mathrm{pol})} = \frac{1}{Z_{\mathrm{FSS}}^{(x,y-\mathrm{pol})}} = Y_0 \frac{1-\Gamma^{(x,y-\mathrm{pol})}}{1+\Gamma^{(x,y-\mathrm{pol})}}; \tag{9.2}$$

Here Y_0 is the intrinsic admittance of the free space and $\Gamma^{(x,y-\mathrm{pol})}$ is the reflection coefficient corresponding to $x-$ or $y-$ polarization respectively, assuming that the cross polarization is small.

9.2 Results

The cost function G was minimized with respect to the thicknesses and permittivities of each layer as well as the resistivity of the lossy sheets. The optimization domain of the parameters is considered as follows:

$$\begin{aligned} 2.2 \le \varepsilon_{r1} \le 6 \qquad & 1.4 \le \varepsilon_{r2} \le 6 \\ 0.6 \le R_1 Y_0 \le 5 \qquad & 0.6 \le R_2 Y_0 \le 5 \\ 2 \le d_1 \le 7 \qquad & 2 \le d_2 \le 7 \end{aligned} \tag{9.3}$$

The final design, using the homogenized FSS-model, was obtained by using the weight $w = 120$. The resulting parameters for this design are $d_1 = 3.0$ mm, $d_2 = 5.7$ mm, $\varepsilon_{r1} = 2.2$, $\varepsilon_{r2} = 1.4$, R_1 =414 $\Omega/\square$ and R_2 =1260 $\Omega/\square$. The corresponding

reflection coefficients for the $x-$ and $y-$ polarizations are illustrated in Fig. 9.4. The transmission coefficient at the transparent window is ~ -4dB. The full-wave results have a good agreement with the results obtained from the propagator model. The structure was investigated in detail in Paper IV. In paper IV, a sensitivity analysis was also accomplished for the rasorber structure. The structure was also applied to an elliptical layer of an aircraft wing front end. It is shown that the absorption characteristics of the structure are robust when it is bent on a curved surface.

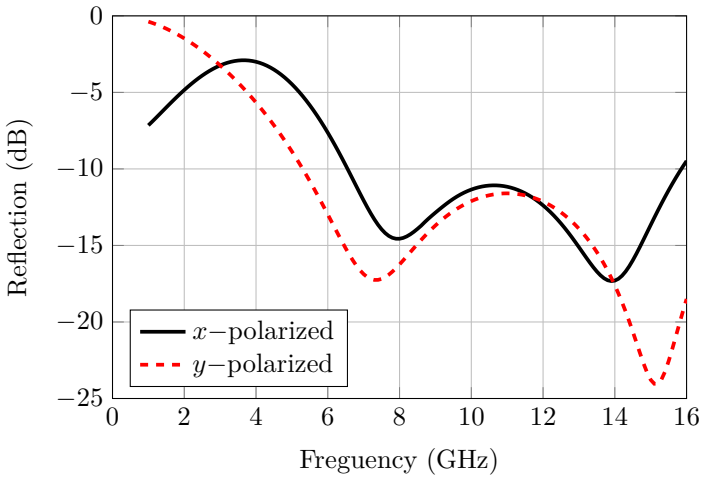

Figure 9.4: The reflection from the FSS-backed Jaumann absorber

One of the important factors in rasorber design is the transmission loss at the transparent window. Using the conservation of power relation for a normally incident plane wave of unit power, the loss of the structure is expressed as

$$P_{\text{loss}}^{x-\text{pol}} = 1 - |\Gamma^{x-\text{pol}}|^2 - |\mathrm{T}^{x-\text{pol}}|^2. \tag{9.4}$$

The resistive loss of the Jaumann-like rasorber at its transparent window (1 GHz) is 43%. This loss could be marginally lowered on the expense of losing part of the absorption bandwidth. However, this level of transmission loss is rather high for a transparent window. In the next chapter, we introduce a different type of rasorber that is based on a capacitive circuit absorber (CCA) [82]. Using a CCA in the rasorber design, the absorption characteristics are improved, transmission coefficient is increased and the loss at the transparent window is decreased. Furthermore, the CCA based design offers a thinner structure than the Jaumann based case.

Chapter 10

Capacitive Circuit Rasorber

It was shown in the previous chapter that the design based on Jaumann-like rasorber suffers from a high transmission loss at its transparent window. This high loss reduces the transmission coefficient at the transparent window, something which is undesired for a rasorber structure. Furthermore, a continuous power transmission through this high loss transparent window can cause problems such as increasing the temperature of the structure and melting. Finally, it is desired to improve the absorption quality of the rasober in the sense of increasing the bandwidth and reducing the reflection coefficient and thickness of the structure.

In this chapter, a different type of rasorber, based on a capacitive circuit absorber (CCA) [82], is introduced. The CCAs are shown to have much better absorption properties than Jaumann absorbers [82–84]. For CCAs, the impedance sheets sandwiched between the two consecutive layers in the stratified absorbers are low-pass resistive-capacitive or series RC circuit element. This impedance can be synthesized by a periodic pattern of resistive patches as shown in Fig. 10.1.

In this Chapter we follow a similar procedure as was used to design a Jaumann-like rasorber, this time for a CCA based rasorber. It will be shown that the rasorber based on a CAA provides better absorption properties and at the same time a lower transmission loss at the transparent window.

10.1 Design

The design goals for the CCA based rasorber are the same as the ones for the Jaumann based rasober described in Chapter 9. Similar to the Jaumann-like rasorber, the back PEC surface of the CCA is replaced with a Gangbuster-Polarizer FSS. By using a denser pattern for the Gangbuster and polarizer FSSs [85], a more selective filtering characteristic for the $x-$ polarization with a sharper transition from transparency frequency region to reflective frequency region is achieved. Furthermore, this new design provides a PEC-like behavior for the $y-$polarized incident waves

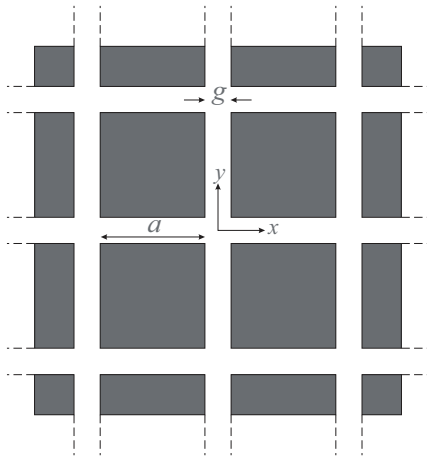

Figure 10.1: Top view of the periodic resistive square patches.

over a wider frequency band. The reflection coefficients from this FSS for the $x-$ and $y-$ polarized incident waves are shown in Fig. 10.2. The values for the parameters of this super dense Gangbuster-Polarizer FSS are presented in the caption of Fig. 10.2.

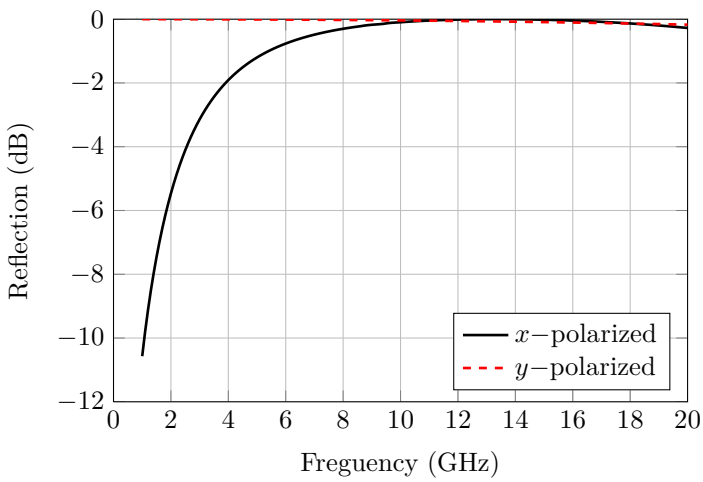

Figure 10.2: The full-wave simulation results for the reflection coefficient of the backing structure. $t = 0.6$ mm, $d_g = 1.6$ mm, $l_d = 8.4$ mm, $b = 1.05$ mm and $s = 0.2$ mm and $\varepsilon_{rs} = 2.5$

The method described in Chapter 8 is employed to analyze the CCA based

rasorber. The circuit model of a two layer CCA rasorber is shown in Fig. 10.3. The normalized equivalent series RC admittance that is sandwiched between layers is given by

$$Y_{sn0} = \frac{Y_{sn}}{Y_0} = \frac{\omega^2 R_{n0} C_{n0}^2}{1 + R_{n0}^2 \omega^2 C_{n0}^2} + \mathrm{j}\frac{\omega C_{n0}}{1 + R_{n0}^2 \omega^2 C_{n0}^2}, \tag{10.1}$$

where $R_{n0} = R_n Y_0$ and $C_{n0} = C_n / Y_0$, n is the number of boundary layers and Y_0 is the intrinsic admittance of the free space. This admittance is implemented in (8.3) as the boundary condition between the consecutive layers. The structure is optimized with a cost function similar to (9.1):

$$G = \sum_{l=10}^{200} \max(\Gamma^{x-\mathrm{pol}}(f_0 + l\Delta f), -20) - w\mathrm{T}^{x-\mathrm{pol}}(f_0), \tag{10.2}$$

where $f_0 = 1$ GHz and $\Delta f = 0.1$ GHz. $\Gamma^{x-\mathrm{pol}}$ and $\mathrm{T}^{x-\mathrm{pol}}$ are respectively, the reflection and transmission coefficient for the x-polarized incidence in dB. The term w is a weight coefficient to make the single transmission coefficient large compared to the summation terms of reflection coefficients. A good compromise between transmission at 1 GHz and absorption over the frequency band 2–20 GHz is obtained by choosing $w = 200$.

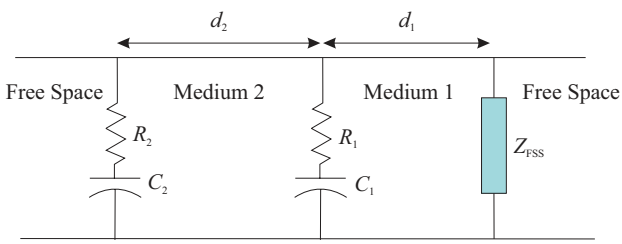

Figure 10.3: Circuit model of a two layer FSS backed capacitive circuit absorber.

The cost function G is minimized with respect to the layer thicknesses,d_1 and d_2, and the admittance parameters R_1, R_2, C_1 and C_2, while the dielectric constant of the medium 1 and 2 layers are fixed at $\varepsilon_{r1} = 2.5$ and $\varepsilon_{r1} = 1.4$ respectively. The function `fmincon` in Matlab 2010 is used for minimizing the cost function G over a range of parameter values. Several starting points are used in order to find the best of the multiple local minima.

10.2 The Synthesis of the Series RC Admittances

The optimization process mentioned in the last section gives the values for capacitances and resistances in the circuit model of the rasorber. This circuit model should be realized as a microwave structure.

The series RC circuits can be synthesized by an FSS pattern of square resistive patches as shown in Fig. 10.1. An electrically dense grid of periodic conductive patches has a capacitance of [86, 87]

$$C = \varepsilon_0(\varepsilon_{rc1} + \varepsilon_{rc2})\frac{a+g}{\pi}\ln(\frac{1}{\sin(\frac{\pi g}{2(a+g)})}), \tag{10.3}$$

provided that $k_{eff}(a+g) \ll 2\pi$. Here, k_{eff} is the wave vector in the dielectric cover of the patches, ε_{rc1} and ε_{rc2} are the relative permittivity of the dielectric cover on the top and bottom sides of the patches and a and g are shown in Fig. 10.1.

The corresponding lumped resistance approximation for a periodic pattern of resistive square patches can also be obtained from [88, 89]

$$R \approx R_s\frac{(a+g)^2}{a^2}, \tag{10.4}$$

where R_s is the resistivity per square of the patch, and a and g are geometric parameters.

The above mentioned formulas can provide an estimate for the lumped R and C values of the periodic pattern of resistive patches. Nevertheless, for a CAA absorber design, a more accurate RC synthesis is required. Such a synthesis can be accomplished by a numerical curve fitting of the reflection coefficient from a series RC circuit and a periodic pattern of resistive patches embedded in a thin dielectric layer. A series RC element in a transmission line with intrinsic impedance η_0 is shown in Fig. 10.4. The voltage reflection coefficient from this RC impedance is given by [60]

$$\Gamma = \frac{Z_L - \eta_0}{Z_L + \eta_0}, \tag{10.5}$$

where

$$Z_L = \left(R + \frac{1}{\mathrm{j}\omega C}\right) \parallel \eta_0. \tag{10.6}$$

Substituting (10.6) into (10.5) and after some algebraic manipulation, the reflection coefficient for the series RC impedance shunted in a transmission line gives

$$\Gamma = \frac{-\mathrm{j}\eta_0 C\omega}{2(\mathrm{j}RC\omega + 1) + \mathrm{j}\eta_0 C\omega}. \tag{10.7}$$

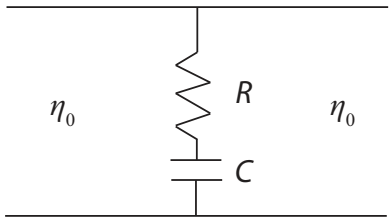

Figure 10.4: A series RC element in a transmission line with intrinsic impedance η_0.

The best values for the patch resistivity, dimension and periodicity are achieved from an optimization process based on the reflection coefficient curve fitting. In this process, the absolute value of the reflection coefficient determined by full-wave analysis of the coated periodic resistive patches are fitted to the corresponding curve achieved from (10.7) with the optimized R and C. Equations (10.4) and (10.3) are used to find an initial value for the patch resistivity, dimension and periodicity in this optimization process.

10.3 Results and Discussion

The Module of Absorption Quality

In general, the desired property for radar absorbers is to provide the lowest possible reflection within the widest operating frequency band, while having the least thickness. However, these requirements are contradictory to each other. In other words, reduction in the absorber's total thickness results in shrinking the absorption bandwidth with a specific value of reflection coefficient. Using the frequency asymptotic behavior of the reflection coefficient [90] and its analytical properties, Rozanov has shown that the integral of the reflection coefficient from a metal back planar multilayer slab, exposed to a normal incident plane wave, over the wavelength is bounded by a theoretical limit [91]

$$|\int_0^\infty \ln|R(\lambda)|\mathrm{d}\lambda| \leq 2\pi^2 \sum_i \mu_{s,i} d_i, \tag{10.8}$$

where $d_i, \mu_{s,i}$ are the thickness and the static permeability of ith layer of the stratified structure and λ is the wavelength in free apace.

If the module of the reflection coefficient of a radar absorber is less than ρ_0 within the operating frequency band $f_{\min} - f_{\max}$, then

$$|\ln(\rho_0)|(\lambda_{\max} - \lambda_{\min}) < |\int_0^\infty \ln|R(\lambda)|\mathrm{d}\lambda|, \tag{10.9}$$

where, $\lambda_{\min}$ and $\lambda_{\max}$ are the wavelength corresponding to $f_{\max}$ and $f_{\min}$ respectively.

From (10.8) and (10.9) and for a non-magnetic absorber we have

$$|\ln(\rho_0)|\frac{\lambda_{\max}-\lambda_{\min}}{\sum_i d_i} < 2\pi^2. \tag{10.10}$$

The left hand side of the inequality (10.10) is the module of absorption. It is a measure of the radar absorber performance. The upper bound of this module of absorption, given by (10.10), gives the ultimate performance of an absorber. This bound can be used to evaluate an absorber design.

Numerical Results

Minimizing the cost function G gives the lumped element values for the circuit model of the rasorber. The resulting values of the optimized parameters are listed in Table 10.1. The circuit model then converted into an equivalent microwave structure using the method described in Section 10.2. As shown in Equation (10.3), the equivalent capacitance depends on the dielectric constant of the coating layers on top and bottom of the resistive patches. In order to have the capacitance unaffected by the permittivity of the rasorber layers, here the patches are coated with an ultra-thin dielectric layer with 0.2 mm thickness at each side. The dielectric constant of the coating for each patch pattern is the same as the dielectric layer below, for example $\varepsilon^i_{rc1} = \varepsilon^i_{rc2} = \varepsilon^i_{rc} = \varepsilon_{ri}$, where i denotes the medium number, 1 or 2, in Fig. 10.3. The parameter values for the final realized microwave structure, equivalent to the RC circuit, with coated periodic resistive patches are shown in Table 10.2.

$R_1(\Omega)$	$R_2(\Omega)$	C_1(pF)	C_2(pF)	d_1(mm)	d_2(mm)
165.4	693.5	0.182	0.031	2.5	3.5

Table 10.1: The optimized parameters for the circuit model shown in Fig. 10.3

$R_{s1}(\Omega/\square)$	$R_{s2}(\Omega/\square)$	ε^1_{rc}	ε^2_{rc}
156	370	2.5	1.4

a_1(mm)	a_2(mm)	g_1(mm)	g_2(mm)
4.76	3.52	0.24	1.48

Table 10.2: The dimensions, resistivity of sheets and cover permittivities of the periodic patches to realized the optimized equivalent lumped values.

The achieved three-dimensional model of the rasorber structure is implemented in Ansoft HFSS 12. A comparison between the homogeneous layer model approximation and the full-wave analysis of the realized structure, both illuminated by a

normal incident wave in either $y-$polarization or $x-$polarization, is shown in Fig. 10.5 and 10.6 respectively. It is shown that the reflection coefficient for the simplified model with stratified homogeneous layers (solid line) agrees well with the reflection coefficient of the full-wave analysis of the realized model (dashed line). The -20 dB absorption bandwidth for the $x-$polarized incidence and -19 dB absorption bandwidth for the $y-$polarized incidence are, respectively, 8.4–19 GHz and 6.6–19.1 GHz.

The values for $x-$ polarized transmitted power at 1 GHz achieved by HFSS and circuit model are -1.9 dB and -1.6 dB, respectively. The designed structure can therefore be classified as an e-class radome [92]. Furthermore, the transmission loss of the structure defined by (9.4) is less than 10%. More details on the design process and results of this CCA rasober together with some perturbation studies, a sensitivity analysis and power handling investigations can be found in **Paper VI**.

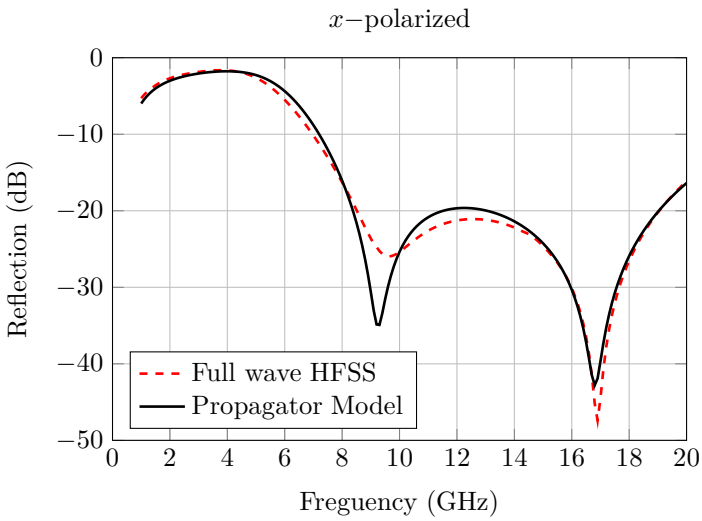

Figure 10.5: Reflection coefficient of the optimized FSS backed CCA absorber for the $x-$polarization

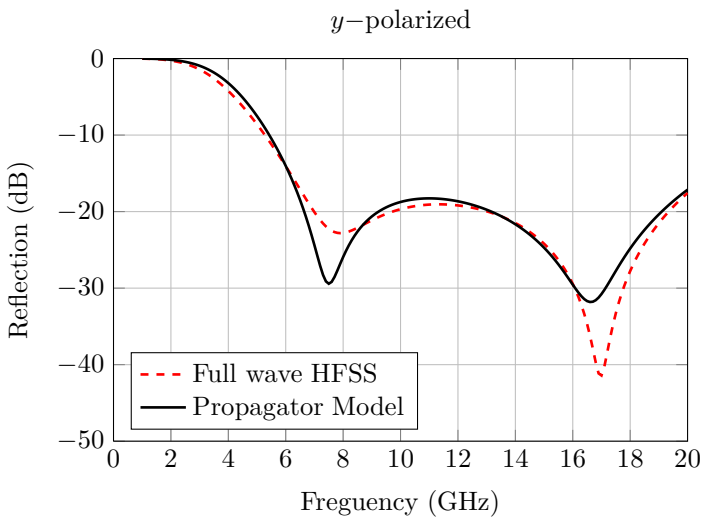

Figure 10.6: Reflection coefficient of the optimized FSS backed CCA absorber for the $y-$polarization

Chapter 11

Conclusion

The second part of this thesis was concerned with designing radar rasorbers. The goal of the project was to design a rasorber structure that is transparent at 1 GHz and lower for one linear polarization while it absorbs, as much as possible, the electromagnetic waves for other frequencies or other polarization. Two rasorber designs, one based on Jaumann and the other based on CCA, were investigated. The wave splitting method was employed to model the rasorber structures. Using this simplified model a fast and efficient method was provided to analyze stratified structures. The structures were optimized using this method and then synthesized using another optimization process. It was shown that The Jaumann-like rasorber design suffers from a high transmission loss at its transparent window. By utilizing a CCA, the transmission loss at the transparent window of the rasorber significantly decreased. At the same time the design based on a CCA gave a larger absorption over a wider bandwidth while having less thickness than the Jaumann-like rasorber. In other words, the rasorber based on a CCA design not only provided a higher transmission with lower transmission loss at its transparent window, but also had a much better module of absorption than the Jaumann-like rasorber.

The Jaumann-like rasorber was also applied to the curved surface of an aircraft wing front. It was shown that the characteristics of the Jaumann-like rasorber persist when it is used on elliptical surface of an aircraft wing front. As future research, the investigation of the characteristics of the CCA rasorber on curved structures would be interesting. The collaboration of the rasorbers located at the near-field region of an antenna is also an interesting future research suggestion. The effects of the rasorber structures on antenna parameters, such as impedance, radiation pattern, and polarization properties, are interesting topics of investigation.

Bibliography

[1] A. Motevsselian, "On the scattering reduction of an aircraft wing profile enclosing an antenna," Licentiate Thesis, Royal Institute of Technology (KTH), Stockholm, Sweden, June 2010.

[2] D. Hondros and P. Debye, "Elektromagnetische wellen an dielektrischen drähten," *Annalen der Physik*, vol. 337, no. 8, pp. 465–476, 1910.

[3] G. E. Mueller and W. A. Tyrrell, "Polyrod antennas," *Bell System Technical Journal*, vol. 337, no. 8, pp. 837–851, 1947.

[4] D. Halliday and D. Kiely, "Dielectric-rod aerials," *Electrical Engineers - Part IIIA: Radiocommunication, Journal of the Institution of*, vol. 94, no. 14, pp. 610 –618, 1947.

[5] R. B. Watson and C. W. Horton, "The radiation patterns of dielectric rods-experiment and theory," *Annalen der Physik*, vol. 337, no. 8, pp. 661–670, Jan. 1948.

[6] C. W. Horton and J. C. M. McKinney, "An experimental investigation of the dielectric rod antenna of circular cross section excited in the dominant mode," *Journal of Applied Physics*, vol. 22, no. 10, pp. 1246–1249, 1951. [Online]. Available: http://link.aip.org/link/?JAP/22/1246/1

[7] G. V. Trentini, "Polystyrene and lucite rod antennas," *Journal of Applied Physics*, vol. 24, no. 7, pp. 960–961, 1953. [Online]. Available: http://link.aip.org/link/?JAP/24/960/1

[8] R. D. Richtmyer, "Dielectric resonators," *Journal of Applied Physics*, vol. 10, no. 6, pp. 391 –398, 1939.

[9] D. Kajfez and P. Guillon, *Dielectric Resonators, 2'nd Edition.* Nobel Publishing Corporation, 1998.

[10] S. Cohn, "Microwave bandpass filters containing high-q dielectric resonators," *Microwave Theory and Techniques, IEEE Transactions on*, vol. 16, no. 4, pp. 218 – 227, 1968.

[11] J. Van Bladel, "On the resonances of a dielectric resonator of very high permittivity," *Microwave Theory and Techniques, IEEE Transactions on*, vol. 23, no. 2, pp. 199 – 208, 1975.

[12] S. A. Long, M. W. McAllister, and L. C. Shen, "The resonant cylindrical dielectric cavity antenna," *IEEE Trans. Antennas Propagat.*, vol. AP-31, no. 3, pp. 406–412, Mar. 1983.

[13] M. W. McAllister and S. A. Long, "Rectangular dielectric resonator antenna," *IEE Electron. Lett.*, vol. 19, pp. 218–219, Mar. 1983.

[14] ——, "Rectangular dielectric resonator antenna," *IEE Electron. Lett.*, vol. 20, pp. 657–659, Aug. 1984.

[15] K. Leung, "Simple result for conformal-strip excited hemispherical dielectric resonator antenna," *Electronics Letters*, vol. 36, no. 11, pp. 933 – 935, May 2000.

[16] K.-W. Leung, K.-M. Luk, K. Lai, and D. Lin, "Theory and experiment of an aperture-coupled hemispherical dielectric resonator antenna," *Antennas and Propagation, IEEE Transactions on*, vol. 43, no. 11, pp. 1192 –1198, Nov. 1995.

[17] A. A. Kishk, A. Ittipiboon, Y. M. M. Antar, and M. Cuhaci, "Slot excitation of the dielectric disk radiator," *IEEE Trans. Antennas Propagat.*, vol. AP-43, no. 2, pp. 198–201, Feb. 1995.

[18] R. Kumar Mongia and A. Ittipiboon, "Theoretical and experimental investigations on rectangular dielectric resonator antennas," *Antennas and Propagation, IEEE Transactions on*, vol. 45, no. 9, pp. 1348 –1356, 1997.

[19] Y.-X. Guo, Y.-F. Ruan, and X.-Q. Shi, "Wide-band stacked double annular-ring dielectric resonator antenna at the end-fire mode operation," *Antennas and Propagation, IEEE Transactions on*, vol. 53, no. 10, pp. 3394 – 3397, 2005.

[20] K. Leung, W. Wong, K. Luk, and E. Yung, "Annular slot-coupled dielectric resonator antenna," *Electronics Letters*, vol. 34, no. 13, pp. 1275 –1277, Jun. 1998.

[21] S.-M. Deng, C.-L. Tsai, S.-F. Chang, and S.-S. Bor, "A cpw-fed suspended, low profile rectangular dielectric resonator antenna for wideband operation," in *Antennas and Propagation Society International Symposium, 2005 IEEE*, vol. 4B, 2005, pp. 242 – 245 vol. 4B.

[22] R. K. Mongia, A. Ittipiboon, Y. M. M. Antar, P. Bhartia, and M. Cuhaci, "A half-split cylindrical dielectric resonator antenna using slot-coupling," *IEEE Microwave and Guided Wave Lett.*, vol. 3, no. 2, pp. 38–39, Feb. 1993.

[23] A. Kishk, "Wide-band truncated tetrahedron dielectric resonator antenna excited by a coaxial probe," *Antennas and Propagation, IEEE Transactions on*, vol. 51, no. 10, pp. 2913 – 2917, 2003.

[24] A. A. Kishk, Y. Yin, and A. W. Glisson, "Conical dielectric resonator antenna for wideband application," *IEEE Trans. Antennas Propagat.*, vol. AP-50, no. 4, pp. 469–474, Apr. 2002.

[25] M. T. K. Tam and R. D. Murch, "Compact circular sector and anular sector dielectric resonator antenna," *IEEE Trans. Antennas Propagat.*, vol. AP-47, no. 5, pp. 837–342, May 1999.

[26] L. Zou and C. Fumeaux, "A cross-shaped dielectric resonator antenna for multifunction and polarization diversity applications," *Antennas and Wireless Propagation Letters, IEEE*, vol. 10, pp. 742 –745, 2011.

[27] Y. Pan and K. W. Leung, "Wideband circularly polarized trapezoidal dielectric resonator antenna," *Antennas and Wireless Propagation Letters, IEEE*, vol. 9, pp. 588 –591, 2010.

[28] L. Chu, D. Guha, and Y. Antar, "Conformal strip-fed shaped cylindrical dielectric resonator: Improved design of a wideband wireless antenna," *Antennas and Wireless Propagation Letters, IEEE*, vol. 8, pp. 482 –485, 2009.

[29] M. Oliver, Y. Antar, R. Mongia, and A. Ittipiboon, "Circularly polarised rectangular dielectric resonator antenna," *Electronics Letters*, vol. 31, no. 6, pp. 418 –419, Mar. 1995.

[30] R. Chair, A. Kishk, and K. Lee, "Wideband dual polarized dielectric resonator antennas at x-band," in *Antennas and Propagation Society International Symposium, 2005 IEEE*, vol. 4B, 2005, pp. 214 – 217 vol. 4B.

[31] Y.-X. Guo and K.-M. Luk, "Dual-polarized dielectric resonator antennas," *Antennas and Propagation, IEEE Transactions on*, vol. 51, no. 5, pp. 1120 – 1124, May 2003.

[32] K. Leung, W. Wong, K. Luk, and E. Yung, "Circular-polarised dielectric resonator antenna excited by dual conformal strips," *Electronics Letters*, vol. 36, no. 6, pp. 484 –486, Mar. 2000.

[33] K. Leung, W. Wong, and H. Ng, "Circularly polarized slot-coupled dielectric resonator antenna with a parasitic patch," *Antennas and Wireless Propagation Letters, IEEE*, vol. 1, no. 1, pp. 57 –59, 2002.

[34] R. Mongia, A. Ittipiboon, M. Cuhaci, and D. Roscoe, "Circularly polarised dielectric resonator antenna," *Electronics Letters*, vol. 30, no. 17, pp. 1361 –1362, 1994.

[35] K. W. Leung and S. K. Mok, "Circularly polarized dielectric resonator antenna excited by a perturbed annular slot with backing cavity," *Electron. Lett.*, vol. 34, no. 13, pp. 934–936, Jul. 2001.

[36] R. K. Mongia and P. Bhartia, "Dielectric resonator antennas-a review and general design relations for resonant frequency and bandwidth," *Int. J. of Microwave and Millimeter-Wave Computer-Aided Engineering*, vol. 4, no. 3, pp. 230–247, May 1994.

[37] A. Petosa, *Dielectric resonator antenna handbook.* Boston: Artech House, 2007.

[38] R. F. Harrington, *Time-Harmonic Electromagnetic Fields.* New York: Wiley-Interscience, 2001.

[39] R. E. Collin, *Field Theory of Guided Waves, 2'nd Edition.* New York: Wiley-Interscience, 1991.

[40] C. A. Balanis, *Antenna Theory: Analysis and Design, 3rd Edition.* New York: Wiley, 1989.

[41] G. L. Yip and T. Auyeung, "Launching efficiency of the he11, surface-wave mode on a dielectric tube," *Microwave Theory and Techniques, IEEE Transactions on*, vol. 22, no. 1, pp. 6 – 14, Jan. 1974.

[42] G. Yip, "Launching of the he11 surface-wave mode on a dielectric rod," *Electronics Letters*, vol. 6, no. 1, pp. 2 –3, Aug. 1970.

[43] G. L. Yip, "Launching efficiency of the he11 surface wave mode on a dielectric rod," *Microwave Theory and Techniques, IEEE Transactions on*, vol. 18, no. 12, pp. 1033 – 1041, Dec. 1970.

[44] G. Yip and T. Au-Yeung, "Launching of the he/sub 11/ surface wave mode by an electric dipole imbedded in a dielectric rod," in *Microwave Symposium, G-MTT 1970 International*, May 1970, pp. 245 –248.

[45] D. G. Kiely, *Dielectric Aerials.* New York: Wiley, 1952.

[46] C. De Young and S. Long, "Wideband cylindrical and rectangular dielectric resonator antennas," *Antennas and Wireless Propagation Letters, IEEE*, vol. 5, no. 1, pp. 426 –429, Dec. 2006.

[47] K. W. Leung, H. Y. Lo, K. M. Luk, and E. K. N. Yung, "Two-dimensional cylindrical dielectric resonator antenna array," *Electron. Lett.*, vol. 34, no. 13, pp. 1283–1285, Jun. 1998.

[48] Y. L. Hu, Z. H. Yang, J. Q. Li, and B. Li, "Backward-wave oscillation suppression in high-power broadband helix traveling-wave tubes," *Electron Devices, IEEE Transactions on*, vol. 58, no. 5, pp. 1562 –1569, May 2011.

[49] P. Jain and B. Basu, "A theory of the attenuator-coated helical slow-wave structure of a traveling-wave tube," *Electron Devices, IEEE Transactions on*, vol. 35, no. 10, pp. 1750 –1757, 1988.

[50] D. A. Watkins, *Topics in Electromagnetic Theory*. New York: Wiley, 1958.

[51] H. Heffner, "Analysis of the backward-wave traveling-wave tube," *Proceedings of the IRE*, vol. 42, no. 6, pp. 930 –937, 1954.

[52] J. D. Kraus, *Antennas, 2nd Edition*. New York: McGraw-Hill, 1988.

[53] Y.-B. Jung and S.-Y. Eom, "Dual-band horn array design using a helical exciter for mobile satellite communication terminals," *Antennas and Propagation, IEEE Transactions on*, vol. 60, no. 3, pp. 1336 –1342, 2012.

[54] P. Cowles and E. Parker, "Helical feeds at millimetre wavelengths," *Electronics Letters*, vol. 7, no. 18, pp. 513 –515, 1971.

[55] R. Johnson and R. Cotton, "A backfire helical feed," *Antennas and Propagation, IEEE Transactions on*, vol. 32, no. 10, pp. 1126 – 1128, 1984.

[56] S. Sensiper, "Electromagnetic wave propagation on helical conductorss," MIT Rresearch Lab, Cambridge, Massachusetts, Tech. Rep. 194, May 1951.

[57] R. Mittra, "Wave propagation on helices," *Antennas and Propagation, IEEE Transactions on*, vol. 11, no. 5, pp. 585 – 586, 1963.

[58] C. A. Balanis, *Antenna Theory: Analysis and Design, 3rd Edition*. New Jersey: Wiley-Interscience, 2005.

[59] W. Hansen and J. Woodyard, "A new principle in directional antenna design," *Proceedings of the Institute of Radio Engineers*, vol. 26, no. 3, pp. 333 – 345, 1938.

[60] D. K. Cheng, *Field and Wave Electromagnetics*. Addison-Wesley Publishing.

[61] R. S. Elliot, *Antenna Theory and Design, Revised Edition*. New Jersey: Wiley-Interscience, 2003.

[62] J. Volakis, *Antenna Engineering Handbook, 4th Edition*. New York: McGraw-Hill, 2007.

[63] H. T. Hui, E. K. N. Yung, and K. W. Leung, "Numerical and experimental studies of a helical antenna loaded by a dielectric resonator," *Radio Sci.*, vol. 32, no. 2, pp. 295 –304, Aug. 1997.

[64] C. Niow, K. Mouthaan, J. Coetzee, and H. Hui, "Design of a small size dielectric loaded helical antenna for satellite communications," in *Microwave Conference, 2009. APMC 2009. Asia Pacific*, 2009, pp. 48 –51.

[65] R. Vaughan and J. Andersen, "Polarization properties of the axial mode helix antenna," *Antennas and Propagation, IEEE Transactions on*, vol. 33, no. 1, pp. 10 – 20, Jan. 1985.

[66] G. Almpanis, C. Fumeaux, and R. Vahldieck, "Offset cross-slot-coupled dielectric resonator antenna for circular polarization," *Microwave and Wireless Components Letters, IEEE*, vol. 16, no. 8, pp. 461 –463, Aug. 2006.

[67] L. Hady, A. Kishk, and D. Kajfez, "Dual-band compact dra with circular and monopole-like linear polarizations as a concept for gps and wlan applications," *Antennas and Propagation, IEEE Transactions on*, vol. 57, no. 9, pp. 2591 –2598, 2009.

[68] A. Bondeson, Y. Yang, and P. Weinerfelt, "Optimization of radar cross section by a gradient method," *Magnetics, IEEE Transactions on*, vol. 40, no. 2, pp. 1260 – 1263, 2004.

[69] P. Ufimtsev, "Comments on diffraction principles and limitations of rcs reduction techniques," *Proceedings of the IEEE*, vol. 84, no. 12, pp. 1830 –1851, Dec. 1996.

[70] B. A. Munk, *Metamaterials: Critique and Alternatives.* pp. 61-70: New York: Wiley, 2009.

[71] ——, *Frequency Selective Surfaces, Theory and Design.* New York: Wiley, 2000.

[72] J. Ramprecht and D. Sjoberg, "On the amount of magnetic material necessary in broadband magnetic absorbers," in *Antennas and Propagation Society International Symposium, 2008. AP-S 2008. IEEE*, 2008, pp. 1 –4.

[73] E. F. Knott, J. F. Shaeffer, and M. T. Tuley, *Radar Cross Section.* Boston: Artech House, 1993.

[74] J. Ramprecht, M. Norgren, and D. Sjöberg, "Scattering from a thin magnetic layer with a periodic lateral magnetization: application to electromagnetic absorbers," *Progress In Electromagnetic Research*, vol. 83, no. 3.

[75] P. Marin, D. Cortina, and A. Hernando, "Electromagnetic wave absorbing material based on magnetic microwires," *Magnetics, IEEE Transactions on*, vol. 44, no. 11, pp. 3934 –3937, Nov. 2008.

[76] J. A. Kong, *Electromagnetic Theory.* New York: Wiley, 1985.

[77] A. Karlsson and G. Kristensson, "Wave splitting in the time domain for a radially symmetric geometry," *Wave Motion*, vol. 12, no. 3, pp. 197–211, 1990. [Online]. Available: http://dx.doi.org/10.1016/0165-2125(90)90039-7

[78] B. L. G. Jonsson and M. Norgren, "Asymptotic wave-splitting in anisotropic linear acoustics," *Wave Motion*, vol. 47, no. 5, pp. 318–326, 2010.

[79] A. K. Bhattacharyya, *Phased Array Antennas*. New York: Wiley-Interscience, 2005.

[80] A. Motevasselian and B. L. G. Jonsson, "Radar cross section reduction of aircraft wing front end," in *Proc. IEEE Int. Conf. on Electromagnetics in Advanced Applications, ICEAA, Turin, Italy*, sep 2009, pp. 237–240.

[81] D. M. Pozar, *Microwave Engineering*. Addison Wesley, 2000.

[82] A. K. Zadeh and A. Karlsson, "Capacitive circuit method for fast and efficient design of wideband radar absorbers," *IEEE Trans. Antennas Propagat.*, vol. AP-57, no. 8, pp. 2307–2314, Aug. 2009.

[83] A. Kazemzadeh and A. Karlsson, "On the absorption mechanism of ultra thin absorbers," *IEEE Trans. Antennas Propagat.*, vol. AP-58, no. 10, pp. 3310–3315, Oct. 2010.

[84] A. Kazemzadeh, "Thin wideband absorber with optimal thickness," in *Electromagnetic Theory (EMTS), 2010 URSI International Symposium on*, Aug. 2010, pp. 676 –679.

[85] S. W. Schneider and B. A. Munk, "The scattering properties of super dense arrays of dipoles," *IEEE Trans. Antennas Propagat.*, vol. AP-42, no. 2, pp. 463–472, Apr. 1994.

[86] O. Luukkonen, F. Costa, C. R. Simovski, A. Monorchio, and S. A. Tretyakov, "A thin electromagnetic absorber for wide incidence angles and both polarizations," *IEEE Trans. Antennas Propagat.*, vol. AP-57, no. 10, pp. 3119–3125, Oct. 2009.

[87] S. Tretyakov, *Analytical Modeling in Applied Electromagnetics*. Boston: Artech House, 2003.

[88] K. W. Whites and R. Mittra, "An equivalent boundary-condition model for lossy planar periodic structures at low frequencies," *IEEE Trans. Antennas Propagat.*, vol. AP-44, no. 12, pp. 1617–1628, Dec. 1996.

[89] F. Costa, A. Monorchio, and G. Manara, "Analysis and design of ultra thin electromagnetic absorbers comprising resistively loaded high impedance surfaces," *IEEE Trans. Antennas Propagat.*, vol. AP-58, no. 5, pp. 1551–1558, May 2010.

[90] L. M. Brekhovskikh, *Waves in layered media*. New York: Academic Press, 1980.

[91] K. N. Rozanov, "Ultimate thickness to bandwidth ratio of radar absorbers," *IEEE Trans. Antennas Propagat.*, vol. AP-48, no. 8, pp. 1230–1234, Aug. 2000.

[92] D. J. Kozakoff, *Analysis of Radome-enclosed Antennas 2'nd Edition.* Boston: Artech House, 2010.

[93] E. Lim, K. Leung, and X. Fang, "The compact circularly-polarized hollow rectangular dielectric resonator antenna with an underlaid quadrature coupler," *Antennas and Propagation, IEEE Transactions on*, vol. 59, no. 1, pp. 288 –293, 2011.

[94] L. Hady, A. Kishk, and D. Kajfez, "Dual-band compact dra with circular and monopole-like linear polarizations as a concept for gps and wlan applications," *Antennas and Propagation, IEEE Transactions on*, vol. 57, no. 9, pp. 2591 –2598, 2009.

[95] A. A. Kishk, "An elliptic dielectric resonator antenna designed for circular polarization with single feed," *Microwave and Optical Technology Letters*, vol. 37, no. 6, pp. 454–456, 2003. [Online]. Available: http://dx.doi.org/10.1002/mop.10948

[96] B. Li, C.-X. Hao, and X.-Q. Sheng, "A dual-mode quadrature-fed wideband circularly polarized dielectric resonator antenna," *Antennas and Wireless Propagation Letters, IEEE*, vol. 8, pp. 1036 –1038, 2009.

[97] K. Leung, "Circularly polarized dielectric resonator antenna excited by a shorted annular slot with a backing cavity," *Antennas and Propagation, IEEE Transactions on*, vol. 52, no. 10, pp. 2765 – 2770, 2004.

[98] K. W. Leung and H. K. Ng, "Theory and experiment of circularly polarized dielectric resonator antenna with a parasitic patch," *Antennas and Propagation, IEEE Transactions on*, vol. 51, no. 3, pp. 405 – 412, 2003.

[99] M. Simeoni, R. Cicchetti, A. Yarovoy, and D. Caratelli, "Plastic-based supershaped dielectric resonator antennas for wide-band applications," *Antennas and Propagation, IEEE Transactions on*, vol. 59, no. 12, pp. 4820 –4825, Dec. 2011.

[100] K.-W. Khoo, Y.-X. Guo, and L. C. Ong, "Wideband circularly polarized dielectric resonator antenna," *Antennas and Propagation, IEEE Transactions on*, vol. 55, no. 7, pp. 1929 –1932, Jul. 2007.

[101] S. Malekabadi, M. Neshati, J. Rashed, and A. Attari, "Circular polarized cylindrical dielectric resonator antenna using a single probe feed," in *Microwave and Millimeter Wave Technology, 2008. ICMMT 2008. International Conference on*, vol. 3, Apr. 2008, pp. 1098 –1101.

[102] B. Li, K. So, and K. Leung, "A circularly polarized dielectric resonator antenna excited by an asymmetrical u-slot with a backing cavity," *Antennas and Wireless Propagation Letters, IEEE*, vol. 2, no. 1, pp. 133 –135, 2003.

[103] C.-Y. Huang, J.-Y. Wu, and K.-L. Wong, "Cross-slot-coupled microstrip antenna and dielectric resonator antenna for circular polarization," *Antennas and Propagation, IEEE Transactions on*, vol. 47, no. 4, pp. 605 –609, 1999.

[104] C.-Y. Huang and C.-W. Ling, "Frequency-adjustable circularly polarised dielectric resonator antenna with slotted ground plane," *Electronics Letters*, vol. 39, no. 14, pp. 1030 – 1031, 2003.

[105] H. Nakano, S. Kirita, N. Mizobe, and J. Yamauchi, "External-excitation curl antenna," *Antennas and Propagation, IEEE Transactions on*, vol. 59, no. 11, pp. 3969 –3977, 2011.

[106] T. A. Latef and S. K. Khamas, "Measurements and analysis of a helical antenna printed on a layered dielectric hemisphere," *IEEE Trans. Antennas Propagat.*, vol. 59, no. 12, pp. 4831 –4835, 2011.

[107] T.-S. Chu and N. Kilcoyne, "The excitation of a dielectric-rod antenna by a helix," *Antennas and Propagation, IRE Transactions on*, vol. 9, no. 4, pp. 416 –417, 1961.

[108] A. Motevasselian, A. Ellgardt, and B. L. G. Jonsson, "A circularly polarized cylindrical dielectric resonator antenna using a helical exciter," *To be Submitted to IEEE Trans. Antennas Propagat.*

[109] M. Heneishi and H. Takazawa, "Broadband circularly polarised palannar array composed of a pair of dielectric resonator antennas," *IEE Electron. Lett.*, vol. 21, pp. 437–438, May 1985.

[110] A. Kishk, B. Ahn, and D. Kajfez, "Broadband stacked dielectric resonator antennas," *Electronics Letters*, vol. 25, no. 18, pp. 1232 –1233, aug. 1989.

[111] P. Hannan, "The element-gain paradox for a phased-array antenna," *IEEE Trans. Antennas Propagat.*, vol. AP-12, no. 4, pp. 423–433, Jul. 1964.

[112] R. J. Dorris, R. T. Long, S. A. Long, M. A. Khayat, and J. T. William, "Mutual coupling between cylindrical probe-fed dielectric resonator antennas," *IEEE Antennas Wireless Propagat. Lett*, vol. 1, pp. 8–9, 2002.

[113] Y. X. Guo, K. M. Luk, and K. W. Leung, "Mutual coupling between millimeter-wave dielectric resonator antennas," *IEEE Trans. Microw. Theory Tech.*, vol. 47, no. 11, pp. 2164–2166, Nov. 1999.

[114] R. Chair, A. A. Kishk, and K.-F. Lee, "Comparative study on the mutual coupling between different sized cylindrical dielectric resonators antennas and circular microstrip patch antennas," *IEEE Trans. Antennas Propagat.*, vol. AP-53, no. 3, pp. 1011–1019, Mar. 2005.

[115] A. Ellgardt and M. Norgren, "Edge element evaluation of tapered-slot elements in phased arrays," in *Antennas and Propagation (EuCAP), 2010 Proceedings of the Fourth European Conference on*, 2010, pp. 1 –5.

[116] ——, "A study of edge effects in triangular grid tapered-slot arrays using coupling coefficients," *Radio Science*, vol. 45, Apr. 2010.

[117] G. P. Junker, A. A. Kishk, and A. W. Glisson, "Input impedance of dielectric resonator antennas excited by a coaxial probe," *IEEE Trans. Antennas Propagat.*, vol. AP-42, no. 7, pp. 960–966, Jul. 1994.

[118] C. Craeye and M. Arts, "On the receiving cross section of an antenna in infinite linear and planar arrays," *Radio Science*, vol. 39, no. 2, Apr. 2004.

[119] E. Knott and K. Langseth, "Performance degradation of jaumann absorbers due to curvature," *IEEE Trans. Antennas Propagat.*, vol. AP-28, no. 1, pp. 137–139, Jan. 1980.

[120] B. Chambers and A. Tennant, "Optimum design of cylindrical Jaumann absorbers," in *Ninth International Conference on Antennas and propagations*, 1995, pp. 450–454.

[121] W. W. Salisbury, "Absorbent body for electromagnetic waves," United States Patent 2,599,944, June 1954.

[122] W. H. Emerson, "Electromagnetic wave absorbers and anechoic chambers through the years," *IEEE Trans. Antennas Propagat.*, vol. AP-21, pp. 484–490, Jul. 1973.

[123] L. J. du Toit, "The design of Jaumann absorbers," *IEEE Antennas Propagat. Mag*, vol. 36, pp. 17–25, Dec. 1994.

[124] F. Sakran, Y. Neve-Oz, M. G. A. Ron, D. Davidov, and A. Frenkel, "Absorbing frequency-selective-surface for the mm-wave range," *IEEE Trans. Antennas Propagat.*, vol. AP-56, no. 8, pp. 2649–2655, Aug. 2008.

[125] "Techniques for analyzing frequency selective surfaces-a review," *Proceedings of the IEEE*, vol. 76, no. 12, pp. 1593 –1615, Dec. 1988.

[126] E. Martini, F. Caminita, M. Nannetti, and S. Maci, "Fast analysis of fss radome for antenna rcs reduction," in *Proc. IEEE Int. Symp. on Antennas and Propagation Society*, July 2006, pp. 1801–1804.

[127] H. Chen, X. Hou, and L. Deng, "Design of frequency-selective surfaces radome for a planar slotted waveguide antenna," *IEEE Antennas and Wireless Propagat. Lett*, vol. 8, pp. 1231–1233, 1980.

[128] C. Sabah1 and S. Uçkun, "Electromagnetic wave propagation through frequency-dispersive and lossy double-negative slab," *Opto-Electronics Review*, vol. 15, no. 3, pp. 133–143, Sep. 2007.

[129] A. Charles, M. S. Towers, and A. McCowen, "Sensitivity analysis of jaumann absorbers," in *Proc. IEE Microwaves, Antennas and Propagation*, August 1999, pp. 257–262.

[130] B. Munk, P. Munk, and J. Prior, "On designing Jaumann and circuit analog absorbers (CA Absorbers) for oblique angle of incidence," *IEEE Trans. Antennas Propagat.*, vol. AP-55, no. 1, pp. 186–193, Jan. 2007.

[131] E. F. Knott and C. D. Lunden, "The two-sheet capacitive Jaumann absorber," *IEEE Trans. Antennas Propagat.*, vol. AP-43, no. 11, pp. 1339–1343, Nov. 1995.

[132] A. Itou, O. Hashimoto, H. Yokokawa, and K. Sumi, "A fundamental study of thin $\lambda/4$ wave absorber using FSS technology," *Electron. Commun. Jpn.*, vol. 87, no. 11, pp. 77–86, 2004.

[133] A. Motevasselian and B. L. G. Jonsson, "A partially transparent Jaumann absorber applied to an aircraft wing profile," in *Proc. IEEE Int. Symp. Antennas and Propagation Society*, July 2010.

[134] ——, "Partially transparent jaumann like absorber applied to a curved structure," *International Journal of Antennas and Propagation*, vol. 2011, 2011. [Online]. Available: http://dx.doi.org/10.1155/2011/708987

[135] F. B. Gross and E. J. Kuster, "An optimized polarization sensitive Salisbury screen," *IEEE Trans. Antennas Propagat.*, vol. AP-35, no. 12, pp. 1492–1495, Dec. 1987.

[136] F. Costa and A. Monorchio, "Absorptive frequency selective radome," in *General Assembly and Scientific Symposium of the International Union of Radio Science (URSI), Proceedings of*, Aug. 2011.

[137] M. Salehi and N. Behdad, "A second-order dual x-/ka-band frequency selective surface," *IEEE Microw. Wireless Compon. Lett.*, vol. 18, no. 12, pp. 785–787, Dec. 2008.

[138] M. A. Al-Joumayly and N. Behdad, "A generalized method for synthesizing low-profile, band-pass frequency selective surfaces with non-resonant constituting elements," *IEEE Trans. Antennas Propagat.*, vol. AP-58, no. 12, pp. 4033–4041, Dec. 2010.

[139] R. E. Collin, *Foundations for Microwave Engineering 2'nd Edition.* pp. 42-43: New York: McGraw-Hill, 1992.

[140] B. A. Munk, R. G. Kouyoumjian, and L. P. Jr., "Reflection properties of periodic surfaces of loaded dipoles," *IEEE Trans. Antennas Propagat.*, vol. AP-19, pp. 612–617, Sep. 1971.

[141] A. Kazemzadeh, "Nonmagnetic ultrawideband absorber with optimal thickness," *IEEE Trans. Antennas Propagat.*, vol. AP-59, no. 1, pp. 135–140, Jan. 2011.